NAVAL POSTGRADUATE SCHOOL

MONTEREY, CALIFORNIA

THESIS

PRINCIPAL COMPONENTS BASED TECHNIQUES FOR HYPERSPECTRAL IMAGE DATA

by

Leonidas Fountanas

December 2004

Thesis Advisor:	Christopher Olsen
Second Reader:	Daphne Kapolka

Approved for public release; distribution is unlimited

THIS PAGE INTENTIONALLY LEFT BLANK

REPORT DOCUMENTATION PAGE	Form Approved OMB No. 0704-0188

Public reporting burden for this collection of information is estimated to average 1 hour per response, including the time for reviewing instruction, searching existing data sources, gathering and maintaining the data needed, and completing and reviewing the collection of information. Send comments regarding this burden estimate or any other aspect of this collection of information, including suggestions for reducing this burden, to Washington headquarters Services, Directorate for Information Operations and Reports, 1215 Jefferson Davis Highway, Suite 1204, Arlington, VA 22202-4302, and to the Office of Management and Budget, Paperwork Reduction Project (0704-0188) Washington DC 20503.

1. AGENCY USE ONLY *(Leave blank)*	2. REPORT DATE December 2004	3. REPORT TYPE AND DATES COVERED Master's Thesis

4. TITLE AND SUBTITLE: Principal Components Based Techniques for Hyperspectral Image Data	5. FUNDING NUMBERS
6. AUTHOR(S) Leonidas Fountanas	
7. PERFORMING ORGANIZATION NAME(S) AND ADDRESS(ES) Naval Postgraduate School Monterey, CA 93943-5000	8. PERFORMING ORGANIZATION REPORT NUMBER
9. SPONSORING / MONITORING AGENCY NAME(S) AND ADDRESS(ES)	10. SPONSORING / MONITORING AGENCY REPORT NUMBER

11. SUPPLEMENTARY NOTES The views expressed in this thesis are those of the author and do not reflect the official policy or position of the Department of Defense or the U.S. Government.

12a. DISTRIBUTION / AVAILABILITY STATEMENT Approved for public release; distribution is unlimited.	12b. DISTRIBUTION CODE A

13. ABSTRACT *(maximum 200 words)*

PC and MNF transforms are two widely used methods that are utilized for various applications such as dimensionality reduction, data compression and noise reduction. In this thesis, an in-depth study of these two methods is conducted in order to estimate their performance in hyperspectral imagery.

First the PCA and MNF methods are examined for their effectiveness in image enhancement. Also, the various methods are studied to evaluate their ability to determine the intrinsic dimension of the data. Results indicate that, in most cases, the scree test gives the best measure of the number of retained components, as compared to the cumulative variance, the Kaiser, and the CSD methods.

Then, the applicability of PCA and MNF for image restoration are considered using two types of noise, Gaussian and periodic. Hyperspectral images are corrupted by noise using a combination of ENVI and MATLAB software, while the performance metrics used for evaluation of the retrieval algorithms are visual interpretation, rms correlation coefficient spectral comparison, and classification. In Gaussian noise, the retrieved images using inverse transforms indicate that the basic PC and MNF transform perform comparably. In periodic noise, the MNF transform shows less sensitivity to variations in the number of lines and the gain factor.

14. SUBJECT TERMS Remote sensing, Hyperspectral imagery, Principal Components Analysis, Minimum Noise Transform.	15. NUMBER OF PAGES 103 16. PRICE CODE

17. SECURITY CLASSIFICATION OF REPORT	18. SECURITY CLASSIFICATION OF THIS PAGE	19. SECURITY CLASSIFICATION OF ABSTRACT	20. LIMITATION OF ABSTRACT
Unclassified	Unclassified	Unclassified	UL

NSN 7540-01-280-5500 Standard Form 298 (Rev. 2-89)
Prescribed by ANSI Std. 239-18

THIS PAGE INTENTIONALLY LEFT BLANK

Approved for public release; distribution is unlimited

PRINCIPAL COMPONENTS BASED TECHNIQUES FOR HYPERSPECTRAL IMAGE DATA

Leonidas Fountanas
Lieutenant, Hellenic Navy
B.S., Hellenic Naval Academy, June 1993

Submitted in partial fulfillment of the
requirements for the degree of

MASTER OF SCIENCE IN APPLIED PHYSICS

from the

NAVAL POSTGRADUATE SCHOOL
December 2004

Author: Leonidas Fountanas

Approved by: Christopher Olsen
Thesis Advisor

Daphne Kapolka
Second Reader

James Luscombe
Chairman, Department of Physics

THIS PAGE INTENTIONALLY LEFT BLANK

ABSTRACT

PC and MNF transforms are two widely used methods that are utilized for various applications such as dimensionality reduction, data compression and noise reduction. In this thesis, an in-depth study of these two methods is conducted in order to estimate their performance in hyperspectral imagery.

First the PCA and MNF methods are examined for their effectiveness in image enhancement. Also, the various methods are studied to evaluate their ability to determine the intrinsic dimension of the data. Results indicate that, in most cases, the scree test gives the best measure of the number of retained components, as compared to the cumulative variance, the Kaiser, and the CSD methods.

Then, the applicability of PCA and MNF for image restoration are considered using two types of noise, Gaussian and periodic. Hyperspectral images are corrupted by noise using a combination of ENVI and MATLAB software, while the performance metrics used for evaluation of the retrieval algorithms are visual interpretation, rms correlation coefficient spectral comparison, and classification. In Gaussian noise, the retrieved images using inverse transforms indicate that the basic PC and MNF transform perform comparably. In periodic noise, the MNF transform shows less sensitivity to variations in the number of lines and the gain factor.

THIS PAGE INTENTIONALLY LEFT BLANK

TABLE OF CONTENTS

I. INTRODUCTION 1
- A. MOTIVATION 1
- B. OBJECTIVES 2
- C. ORGANIZATION OF THE REPORT 3

II. FUNDAMENTALS OF HYPERSPECTRAL REMOTE SENSING 5
- A. BASIC CONCEPTS 5
  - 1. Hyperspectral Remote Sensing 5
  - 2. Characteristics of Electromagnetic Radiation 7
  - 3. Remote Sensing Systems and Applications 9
- B. IMAGING PROCESSING SYSTEMS 11
- C. IMAGE DISTORTIONS IN HYPERSPECTRAL REMOTE SENSING DATA 16
  - 1. Atmospheric Distortions 17
  - 2. Instrumental Distortions 19
  - 3. Geometric Distortions 20
  - 4. Noise Modeling 21

III. PRINCIPAL COMPONENTS ANALYSIS 25
- A. OVERVIEW 25
  - 1. Basic Principal Components Analysis 26
  - 2. Minimum Noise Fraction Transform 33
- B. APPLICATION OF PCA TECHNIQUES 34
  - 1. Determining the Intrinsic Dimension of Data 35
  - 2. Basic Principal Components Analysis 39
  - 3. MNF Transform 47

IV. NOISE REDUCTION USING PCA TECHNIQUES 55
- A. METHODOLOGY 55
  - 1. Overview 55
  - 2. Performance Metrics 55
- B. IMAGE RESTORATION - RANDOM NOISE 57
- C. IMAGE RESTORATION IN PERIODIC NOISE 71

V. CONCLUSIONS 79

LIST OF REFERENCES 83

INITIAL DISTRIBUTION LIST 85

THIS PAGE INTENTIONALLY LEFT BLANK

LIST OF FIGURES

Figure 1. Typical pixel's spectrum from multispectral and hyperspectral images. 6
Figure 2. A typical hyperspectral Airborne Visible/Infrared Imaging Spectrometer (AVIRIS) datacube of 224 bands from Jasper Ridge in California. 6
Figure 3. Wavelength regions of the electromagnetic spectrum.[From 23].....7
Figure 4. Hyperspectral pixel spectra. 9
Figure 5. Representative algorithm chain for hyperspectral image exploitation. 11
Figure 6. An AVIRIS image of 224 bands (red 647.05 nm, green 549.23 nm, blue 451.22 nm). 14
Figure 7. A HYDICE image of 210 bands (red 745.364 nm, green 647.131 nm, blue 450.257 nm). 15
Figure 8. A Hyperion image of 242 bands (red 752.97 nm, green 651.28 nm, blue 447.89 nm). 16
Figure 9. Characteristics of absorption by atmospheric molecules. [From 24] 18
Figure 10. Effects of platform position and attitude errors on the region of earth being imaged, when these errors occur slowly compared with image acquisition [From 2]. 22
Figure 11. Histogram of a Gaussian noise function. 23
Figure 12. Data in a PC example (a) original data and their means (b) normalized data with the eigenvectors of the covariance matrix overlaid.....29
Figure 13. (a) Derived data set using both components (b) Derived data set using only one component. 31
Figure 14. Eigenvalue plots of the AVIRIS image. 32
Figure 15. Scree graph of the first 25 eigenvalues of the correlation matrix for the AVIRIS, HYDICE, and Hyperion images. 36
Figure 16. Principal component images for AVIRIS, HYDICE, and Hyperion data using the correlation matrix corresponding to the PCs that should be retained based on different methods. 38
Figure 17. Scatter plots of original image data (a) AVIRIS band 1 versus band 2 and, (b) HYDICE band 1 versus band 2. 39
Figure 18. Scree graph for AVIRIS data using the covariance matrix (a) 224 eigenvalues and, (b) the first 25 eigenvalues (y-axis is logarithmic). 40
Figure 19. First 24 PC images of AVIRIS image data. 42
Figure 20. Scatter plots of PC bands of AVIRIS image data (a) band 1 versus band 2 and, (b) band 2 versus band 3. 42
Figure 21. Scree graph for HYDICE data using the covariance matrix (a) 220 eigenvalues and, (b) the first 25 eigenvalues (y-axis is logarithmic). 43
Figure 22. First 24 PC images of HYDICE image data. 44
Figure 23. Scree graph for Hyperion data using the covariance matrix (a) 210 eigenvalues and, (b) the first 25 eigenvalues (y-axis is logarithmic). 45
Figure 24. First 24 PC images of Hyperion image data. 46
Figure 25. First 24 MNF images of AVIRIS image data. 51
Figure 26. First 24 MNF images of HYDICE image data. 52
Figure 27. First 25 MNF images of Hyperion image data. 53

Figure 28. Representative block diagram of noise reduction techniques. 56
Figure 29. The 20th band of the AVIRIS images: a) original b) noisy with variance 300 and c) noisy with variance 600. 58
Figure 30. The first 7 PC components of the AVIRIS images: (a) original (b) noisy with variance 300 and (c) noisy with variance 600. 59
Figure 31. The first 7 MNF components of the AVIRIS images: (a) original (b) noisy with variance 300 and (c) noisy with variance 600. 61
Figure 32. Scatter plots of MNF bands of AVIRIS original vs. noisy with variance 600 image data (a) band 1 vs. band 1, (b) band 2 vs. band 2 and, (c) band 3 vs. band 3. 62
Figure 33. Spectra from an open sea area from the AVIRIS image for the original, noisy, and retrieved spectra using PCA and MNF transformation (bands 1 to 20 (upper figure) and bands 45 to 65 (lower figure)). 64
Figure 34. The 10th band of the follow HYDICE images: (a) original (b) noisy with variance of 300 (c) retrieved using PCA and keeping 5 components and, (d) retrieved using MNF and keeping 6 components.....65
Figure 35. The first 5 PC components of the AVIRIS images: (a) noisy with variance 300 in all bands (b) noisy with variance 300 in all bands except band 20 in which variance is 600 and (c) noisy with variance 300 in all bands except band 20 in which variance is 900.....67
Figure 36. The 20th band of the follow AVIRIS images: (a) original without noise (b) noisy with variance 300 in all bands except band 20 in which variance is 900 and (c) retrieved image by keeping the 1st, 2nd, 4th, and 5th principal components (d) retrieved image by keeping the first five components. 69
Figure 37. The scatter plots of the 20th band (588.5800 nm) between the original AVIRIS image and the following images: (a) noisy with variance 300 in all bands except band 20 in which variance is 900 and (b) retrieved PCA image keeping the 1st, 2nd, 4th, and 5th components (c) retrieved PCA image keeping the first five components and (d) retrieved MNF image keeping the first six components.....70
Figure 38. AVIRIS classification images using a simple classifier: (a) original image (b) noisy image with variance 300 (c) inversed PCA image retaining five components. 72
Figure 39. The 20th band (588.5800 nm) of an AVIRIS image: (a) original image data (b) corrupted image data with 3 horizontal lines of gain factor 1.5.....73
Figure 40. The first six PC components of an AVIRIS image that has been corrupted by three horizontal lines in each band from 11th to 30th for two different gain factors: (a) gain factor 1.3 (the two left columns) and (b) gain factor 2.0 (the two right columns).....74
Figure 41. The 20th band of an AVIRIS image that have been corrupted by three lines in bands 11 to 30 using an offset factor of 2,000. Image data have been restored as follows: (a) using PCA transformation and retaining 5 components, and (b) using MNF transformation and retaining 8 components. 75

Figure 42. The 20th band of an AVIRIS image that has been corrupted by 3 horizontal lines with offset values +2,000 and +3,000 for the images (a) and (b), respectively. 76
Figure 43. The 20th band of an AVIRIS image that have been corrupted by three lines in bands 11 to 30 using an offset value of 2,000. Image data have been restored as follows: (a) using PCA transformation and retaining 3 components, and (b) using MNF transformation and retaining 8 components. 77
Figure 44. The first ten PCA and MNF components of an AVIRIS image that has been corrupted by three horizontal lines in each band from the 11th to 30th with an offset value of 2,000....78

THIS PAGE INTENTIONALLY LEFT BLANK

LIST OF TABLES

Table 1. Eigenvalues and cumulative percentage of the correlation matrix for AVIRIS, HYDICE, and Hyperion images. 37
Table 2. Intrinsic dimension (retained PC's) for AVIRIS, HYDICE, and Hyperion images for all methods. 37
Table 3. Eigenvalues and cumulative percentage of the covariance matrix in the basic PCA transform for AVIRIS, HYDICE, and Hyperion images. 48
Table 4. Eigenvalues and cumulative percentage of the covariance matrix of MNF transformation for AVIRIS, HYDICE, and Hyperion images. 50
Table 5. RMS correlation coefficients for original vs. retrieved AVIRIS image data using PCA or MNF transform for two values of noise variance, 300, and 600. 63
Table 6. RMS correlation coefficients for original vs. retrieved HYDICE and Hyperion image data using PCA or MNF transform for noise variance, 300 and 150 respectively. 65
Table 7. RMS correlation coefficients for original vs. retrieved image data using PCA or MNF transform for noise variance 300 in all bands except of 20th band in which variance is 600 or 900. In PC 1 all the components are retained while in PC 2 the noisy component is excluded. 68

THIS PAGE INTENTIONALLY LEFT BLANK

LIST OF ABBREVIATIONS

AVHRR	Advanced Very High Resolution Radiometer
ASCII	American Standard Code for Information Interchange
ATREM	Atmosphere Removal
AVIRIS	Airborne Visible/Infrared Imaging Spectrometer
BIL	Bands Interleaved by Lines
BIP	Bands Interleaved by Pixels
CSD	Continuous Significant Decomposition
ENVI	Environment for Visualizing Images
EOF	Empirical Orthogonal Function
HYDICE	Hyperspectral Digital Imagery Collection Experiment
IFOV	Instantaneous Field of View
IR	Infrared
MB	Megabyte
MNF	Minimum Noise Fraction
NAPC	Noise Adjusted Principal Components
NASA	National Aeronautics and Space Administration
PC	Principal Component
PCA	Principal Component Analysis
RMS	Root Mean Square
SAM	Spectral Angle Mapper
SAR	Simultaneous Autoregressive
SVD	Singular Value Decomposition
SNR	Signal to Noise Ratio
UV	Ultraviolet

THIS PAGE INTENTIONALLY LEFT BLANK

I. INTRODUCTION

A. MOTIVATION

There are strong motivations for acquiring information remotely in both civilian and military applications. The need to track changes in the environment, as with the need to acquire information of military relevance, motivates the field of remote sensing. The discipline can trace its origins to aerial photography as far back as the American Civil War, when aerial photographs were taken from balloons – an approach that continued into World War I. Technological advances made possible the use of infrared (IR) and microwave electromagnetic radiation during World War II. Following World War II, rapid advances in remote sensing technology were achieved. The concurrence of three developments enabled these advances: the advent of orbiting spacecraft, digital computing, and pattern recognition technology [10]. In 1972, the launch of the Earth Resources Technology Satellite (later renamed Landsat 1) marked the advent of remote sensing from space using multispectral sensors. The founders of the field made an early decision that space-based remote sensing would focus on spectral variations instead of spatial characteristics in imagery (David Landgrebe, Landgrebe Symposium 2003).

This paradigm for remote sensing makes use of the material-dependent character of the observed radiation reflected or emitted from materials depending on their molecular composition and shape. Beginning in the 1980's, spectral imagery evolved from the multispectral world of Landsat and Advanced Very High Resolution Radiometer (AVHRR) to the higher dimensionality of hyperspectral systems.

Multispectral sensors (e.g. Landsat, AVHRR) measure radiation reflected at a few wide, separated spectral bands – typically 5 to 7 bands. Hyperspectral sensors measure reflected radiation at a series of narrow and contiguous spectral bands – typically hundreds of bands. This characteristic of hyperspectral imagery provides the potential for more accurate and detailed information extraction.

Hyperspectral imagery contains a wealth of data, but interpreting it is a difficult task for several reasons. First, the data volume can be quite large – often 100's of megabytes (MB) per scene. Second, data are distorted by additive noise from the

atmosphere, the instrument making the measurements, and the data quantization procedure. Finally, the spectrum of a pixel usually contains the response to more than one material - that is the pixels are not pure. The analysis process is characterized by data that contain a high degree of redundancy. These characteristics motivate a need for preprocessing techniques to facilitate the effective analysis of hyperspectral image data.

The analysis of spectral imagery typically requires atmospheric compensation, dimensionality reduction, and image enhancement. The purpose of implementing these procedures is to facilitate usage of spectral libraries, to reduce the computational complexity and to eliminate noise. A fundamental principle when implementing these procedures is that all the useful information must be preserved.

One of the most well-known techniques for dimensionality reduction while preserving the information in hyperspectral data is the principal components analysis (PCA) family of techniques. Additionally, PCA techniques have proven effective in the noise reduction of image data.

Based on the above considerations, the motivation of this thesis is to investigate the applicability of the principal components analysis techniques in dimensionality reduction and image enhancement in order to enable improved analysis and information extraction from spectral imagery.

B. OBJECTIVES

The objective of this thesis is to conduct an in-depth study of the principal components family of techniques as applied to hyperspectral data for compression and noise reduction. More specifically, research goals can be summarized as follows:

- To investigate the applicability of PCA-based techniques for dimensionality reduction.
- To compare Principle Components (PC) and Minimum Noise Fraction (MNF) methods in reducing noise from hyperspectral images.
- To address the issue of determining the intrinsic dimension of data.

C. ORGANIZATION OF THE REPORT

This thesis is organized as follows: Chapter II discusses the fundamental concepts of hyperspectral remote sensing by emphasizing the analysis of the noise that is contained in hyperspectral images. Chapter III, describes the two PCA methods investigated in this thesis, principal components (PC) and minimum noise fraction (MNF), and studies the application of principal components analysis techniques in hyperspectral images for dimension reduction without the loss of significant information. Also, methods for determining the intrinsic dimension of data are explored. Chapter IV examines the applicability of PC and MNF for image restoration, considering two types of noise, Gaussian and periodic. Chapter V provides concluding remarks and suggestions for future work.

THIS PAGE INTENTIONALLY LEFT BLANK

II. FUNDAMENTALS OF HYPERSPECTRAL REMOTE SENSING

A. BASIC CONCEPTS

1. Hyperspectral Remote Sensing

Spectral images are collected by remote sensing instruments, which are typically carried by airplanes or satellites. As these platforms move along their flight paths, the instruments scan across a swath perpendicular to the direction of motion. The data from a series of such swaths form a two-dimensional image.

Sensors that collect remote sensing data are typically opto-electronic systems that measure reflected solar irradiance. Spectral imagers record this reflected energy at a variety of wavelengths. Early earth imaging systems, such as Landsat, did this in a few relatively broad bands that were not-contiguous, that is, there were gaps in the spectral coverage. Hyperspectral sensors typically measure brightness in hundreds of narrow, contiguous wavelength bands so that for each pixel in an image, a detailed spectral signature can be derived. The term hyperspectral is used to reflect the large number of bands, but the contiguous (complete) spectral coverage is also an important component to the definition. The bands need to be narrow enough to resolve the spectral features for targets of interest, a requirement that can lead to bands from a few nanometers in width to tens of nanometers.

Figure 1 illustrates the different characteristics of multispectral and hyperspectral data, and the differing spectral resolution. A hyperspectral image can be viewed as a cube with spatial information represented in the X-Y plane. The third dimension, which is the Z-direction, is the spectral domain represented by hundreds of narrow, contiguous spectral bands corresponding to spectral reflectance. Figure 2 shows a representative hyperspectral image, or hypercube, with spatial dimensions 1024 by 614, and spectral data of 224 contiguous bands, from 0.4 μm to 2.5 μm. This image is a red, green, blue composite formed using bands 43 (769.68 nm), 17 (539.40 nm), and 10 (470.76 nm).

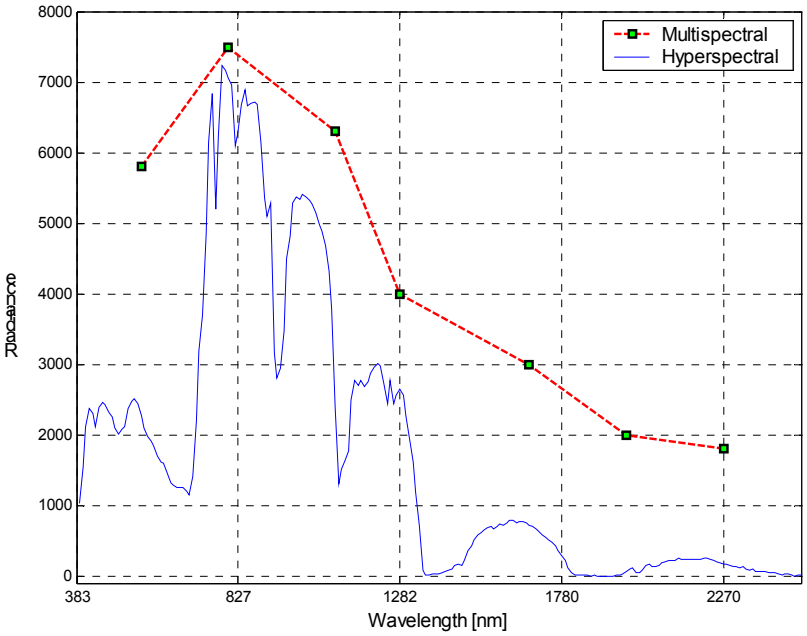

Figure 1. Typical pixel's spectrum from multispectral and hyperspectral images.

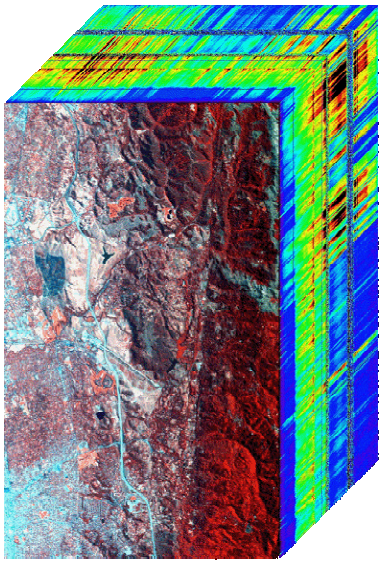

Figure 2. A typical hyperspectral Airborne Visible/Infrared Imaging Spectrometer (AVIRIS) datacube of 224 bands from Jasper Ridge in California.

2. Characteristics of Electromagnetic Radiation

Hyperspectral imagery involves the sensing of electromagnetic radiation. The electromagnetic spectrum that is used in remote sensing includes the ultraviolet (UV), visible, infrared, and microwave portions of the spectrum. Figure 3 illustrates the wavelength regions of the electromagnetic spectrum. The spectral portions of near IR and short wave infrared (0.7-3.0 μm) are called the reflective infrared because measured radiation in this spectral region is mostly composed of reflected sunlight. In contrast, the IR spectrum from 5.0 to 13.0 μm is termed thermal infrared because measurements in this spectral region are generally recording energy radiated from scene elements.

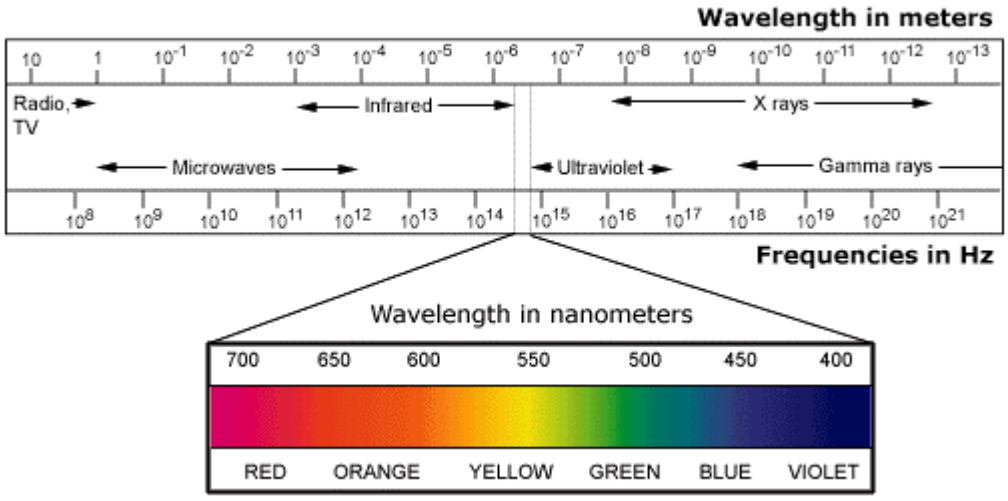

Figure 3. Wavelength regions of the electromagnetic spectrum. [From 23]

Based on these wavelength regions, remote sensing can be classified into three main categories: visible and reflective infrared remote sensing, thermal remote sensing, and microwave remote sensing. In visible and reflective remote sensing, the radiation that is measured has a solar origin, radiated with a peak wavelength of 0.5 μm. In thermal remote sensing, the measured radiation comes from the observed objects. Materials with normal temperatures (~300K) emit radiation with a peak wavelength of 10.0 μm. Finally, in microwave remote sensing, observations are generally due to

reflection of energy radiated by the observing platform (i.e. radar). In this thesis, hyperspectral images from the visible and reflective infrared spectrum are used. The majority of currently available sensors with material identification (ID) capability utilize this portion of spectrum.

Typically the source of energy in hyperspectral imagery is the sun. The incident energy from the sun that is not absorbed or scattered in the atmosphere interacts with the earth's surface, where it is absorbed, transmitted, or reflected. Additionally, the electromagnetic radiation has specific properties that are predictable in its interaction with materials and transmission through the atmosphere. Therefore, by measuring the electromagnetic radiation in narrow wavelength bands, the resulting spectral signatures can be used, in principle, to uniquely characterize and identify any given material [9].

All materials have unique spectral characteristics because they absorb, reflect, and emit radiation in a unique way. For example, in the visible portion of the spectrum, a leaf appears green because it absorbs in the blue and red regions of the spectrum and reflects in the green region. These variations in absorption, reflection, and emission are due to the material composition. Differences in spectral response due to absorption, transmission, and reflection cause materials to have a unique spectral signature. Figure 4 illustrates the spectral signatures of three pixels, respectively dominated by seawater, vegetation, and concrete. Comparing the spectra between seawater and vegetation, it is observed that they reflect similarly in the visible wavelengths but differently in the infrared portion. Also, concrete has a different spectral signature compared to the other two in specific wavelength regions. Therefore, by knowing a material's spectral signature, it is possible for this material to be detected in pixels within an image. Libraries with the characteristic spectra of various materials of interest exist, and these spectral signatures can be compared with measured spectra in order to identify the features in an image. In the early work on spectral imagery, computational limits prevented full exploitation of such data. Computational power in the latter portion of the 1990’s made routine use of spectral imagery much more practical.

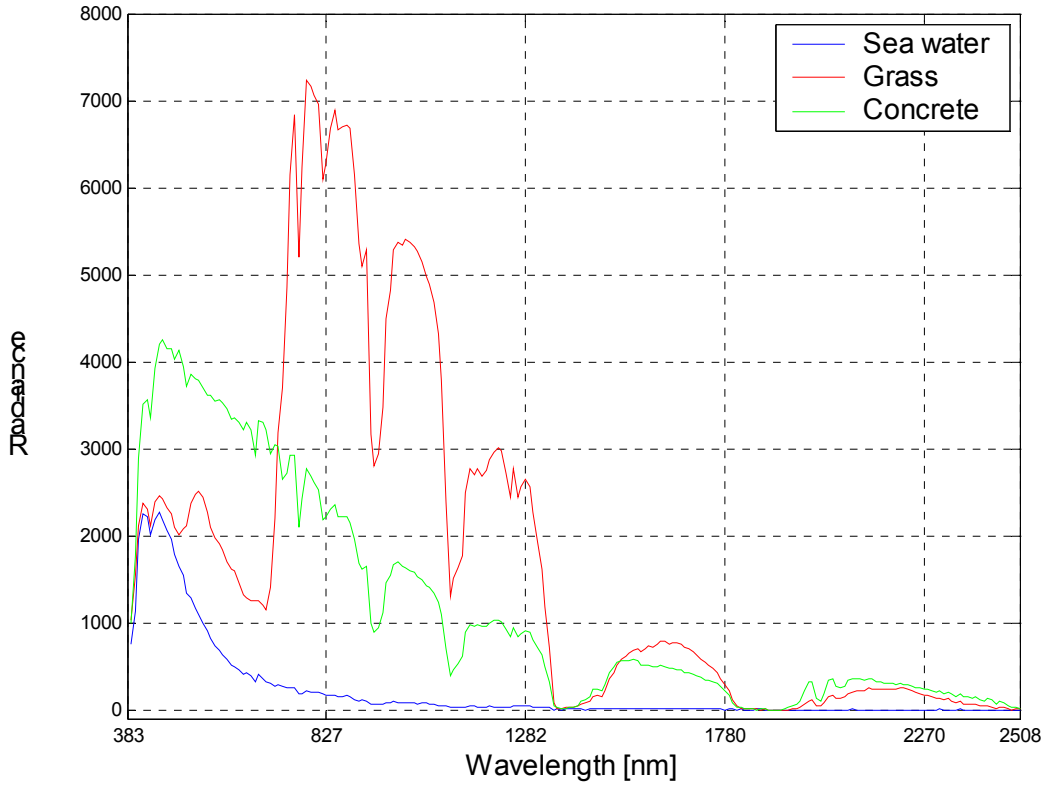

Figure 4. Hyperspectral pixel spectra.

3. Remote Sensing Systems and Applications

Hyperspectral sensors oversample the spectrum signal in contiguous bands to ensure that features are well represented. This oversampling, and the wide frequency range of the energy reflected from the ground, result in hyperspectral data with a high degree of spectral redundancy [1]. Additionally, the interpretation of data is not an easy task because of computational complexity. Typically, a hyperspectral image occupies more than 100 MB, which makes the processing of the data a slow procedure even with a modern computer. Also, data are distorted by additional effects from the atmosphere and other types of noise, which are explained in following sections. Identification of materials becomes more complex because a pixel, which is the lowest possible measured area, typically contains more than one material, which means it is a "mixed" pixel. The spectral signature of a mixed pixel is formed by the combination of the existing materials within the pixel.

Based on the above considerations, analysis of spectral imagery consists of several steps of processing the data for effective interpretation. Figure 5 provides a simplified block diagram of the processing chain involved in the analysis of hyperspectral images.

The first step in processing hyperspectral image data is atmospheric compensation, a procedure that accounts for the atmospheric effects. Data are converted from at-sensor radiance to reflectance, to facilitate comparison to known spectral signatures, typically found in libraries or known from ground truth exercises conducted in parallel with flight experiments. Conversion from radiance to reflectance can be done in a variety of ways, all giving slightly different results. One popular method of doing the conversion is to divide the radiance observations by the scene's average spectrum. For the purposes of this study, it is important to note that atmospheric compensation is connected to the noise level for the spectral data.

After correcting atmospheric effects, dimensionality reduction and image enhancement are performed to reduce the level of redundancy and noise. These operations include functions that assist in the analysis and information extraction of the images. Image enhancement mainly improves the appearance of the imagery for better visual interpretation, while transformations produce new images from the original bands in order to highlight certain features. The hyperspectral data are transformed to a new space with fewer spectral bands, with the expectation that detection performance and resolution between different features can be improved.

Finally, data are ready for information extraction based on end-user needs. Currently, hyperspectral remote sensing is used in a variety of applications. In these applications, the final processes that take place are unmixing and detection. Unmixing is the procedure by which the measured spectrum of a mixed pixel is decomposed into a collection of constituent spectra, or end members [22]. Detection is accomplished by comparing the hyperspectral signatures from library data to the measured data. The first process, unmixing, is done mainly using classification procedures. Classification is a

process that organizes pixels into groups with, more or less, spectral similarity, based on the principle that different features have unique reflectance signatures across the electromagnetic spectrum [15].

The processes of unmixing and detection help users in three main applications: target detection, material identification, and material mapping. In target detection, the purpose is the detection of materials with a known spectral signature or the detection of anomalous elements, not related to the background scene. More broadly, in material identification projects the materials in the scene are not known. The analysis aims to identify the unknown materials within the scene. Similarly, in material mapping the location of materials within the scene are not known. Geologists use material mapping techniques to map out where various minerals exist in a scene.

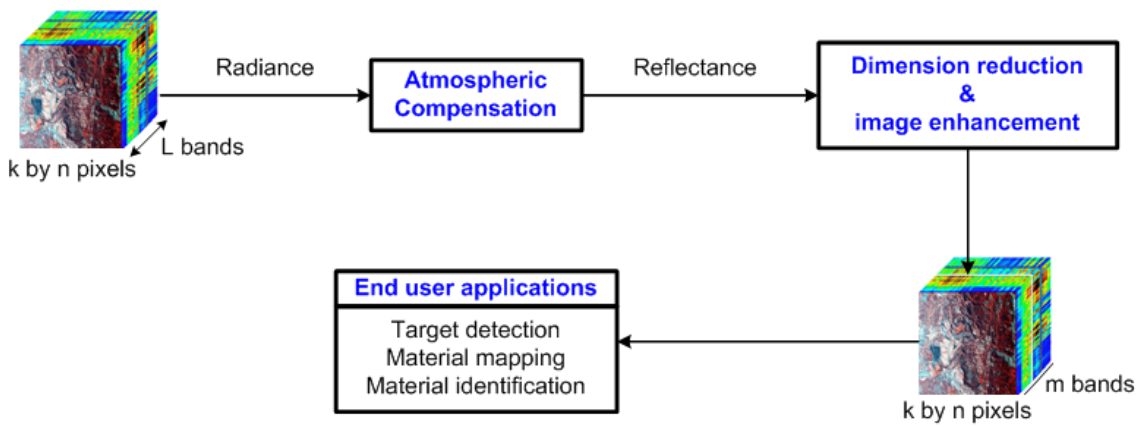

Figure 5. Representative algorithm chain for hyperspectral image exploitation.

B. IMAGING PROCESSING SYSTEMS

Remote sensing systems are divided into two main categories: passive and active. Passive systems have sensors that detect energy naturally available, while active sensors provide their own energy source for illumination. The sun is the main source for passive sensors working in the visible and short-wave infrared (SWIR). Sensors working in the mid-wave infrared (MWIR) and long wave infrared (LWIR) react to the energy radiated

by scene elements. By contrast, active sensors emit radiation to the target and measure the reflected radiation. In this thesis only hyperspectral images collected from passive sensors are used.

The sensors used in remote sensing have three main characteristics: spatial, spectral, and radiometric resolution. Spatial resolution refers to the smallest possible feature that can be detected and mainly depends on the sensor's Instantaneous Field of View (IFOV). The IFOV is defined as the angular cone of visibility of a sensor, and it determines the area on the Earth's surface, as seen from a given altitude, at a particular moment in time [12]. For example, assuming a flight altitude of 1,000 m and an IFOV of 2.5 milliradians, the detected area on the ground will be 2.5 meters by 2.5 meters, which is the sensor's maximum spatial resolution or the resolution cell. In target detection and classification, a feature should have a size larger than the resolution cell - or its radiance should dominate the cell - in order to be detected. (Sub-pixel techniques allow detection of objects smaller than the resolution cell, but the confidence level drops.) Depending on the application, either the detail associated with one pixel, or the information from the total area imaged by the sensor may be needed. Generally, in military applications high resolution is desirable, while in many commercial applications the coverage of large areas is more important.

Spectral resolution refers to the ability to distinguish closely spaced wavelengths. Multi-spectral sensors measure brightness over a few separable wavelength ranges, typically using 4 to 30 bands. Hyperspectral sensors have hundreds of narrow contiguous spectral bands throughout the visible, near infrared, and short wave infrared portions of electromagnetic spectrum. The high spectral resolution allows for better discrimination among different features in the image.

Radiometric resolution refers to the ability of a sensor to discriminate differences in measured brightness. High radiometric resolution means that the sensor can distinguish very slight differences in radiation. This resolution is determined by the number of available brightness levels. This number is defined by the number of coding

bits used for representation of the image. For example, a sensor that uses 8 bits has 2^8 = 256 discrete brightness levels. Radiometric resolution affects the amount of detail contained in a scene.

In this thesis three types of images are used for processing and analysis: Airborne Visible/Infrared Imaging Spectrometer (AVIRIS), Hyperspectral Digital Imagery Collection Experiment (HYDICE) and Hyperion data. Color composites of the AVIRIS, HYDICE, and Hyperion images used in experiments for this thesis are shown in Figures 6, 7 and 8, respectively.

AVIRIS [13] is a unique optical imaging sensor that delivers calibrated images of the upwelling spectral radiance in 224 contiguous spectral channels with wavelengths from 0.4 to 2.5 μm. It has been the state of the art spectral imaging system since 1987. The main objective of the AVIRIS project is to identify, measure, and monitor constituents of the Earth's surface and atmosphere based on molecular absorption and particle scattering signatures. AVIRIS has been flown on two aircraft, the NASA ER-2 and the Twin Otter. The NASA ER-2, a modified U2 aircraft, flies at approximately 20 km above sea level at about 730 km/hour and has a ground swath and ground sampling distance of approximately 11 km and 17 m, respectively. Higher spatial resolution AVIRIS data have become available in recent years as the system has been reconfigured to allow flight on low-altitude aircraft, particularly the Twin Otter, flying at 4 km above ground level at 130 km/hour.

Figure 6. An AVIRIS image of 224 bands (red 647.05 nm, green 549.23 nm, blue 451.22 nm).

HYDICE was designed and developed by Hughes-Danbury Optical Systems Inc., in order to provide high quality hyperspectral data to explore techniques for a wide variety of applications [16]. It was designed with the intention of collecting somewhat higher spatial-resolution imagery than AVIRIS and uses a 2-D focal plane for push-broom imaging, in contrast to the AVIRIS linear array which operates in whisk-broom mode. The pushbroom scanner, also referred to as an along-track scanner, has an optical lens through which a line image is formed perpendicular to the flight direction. The whiskbroom scanner, also referred to as across-track, uses rotating mirrors to scan the landscape below from side to side perpendicular to the direction of the sensor platform. The HYDICE sensor operates in the spectrum from 0.4 to 2.5 μm, which is sampled into 210 contiguous bands, with a spectral width of ~10 nm for each band.

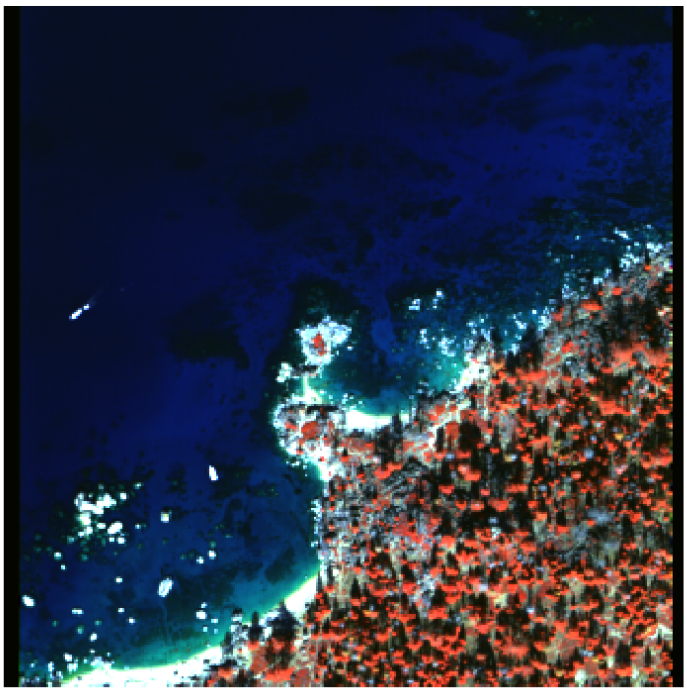

Figure 7. A HYDICE image of 210 bands (red 745.364 nm, green 647.131 nm, blue 450.257 nm).

Finally, the Hyperion sensor, flown aboard NASA's Earth Observation-1 satellite, provides a high resolution hyperspectral imager capable of resolving 196 spectral bands in wavelength ranges of 10 nm (from 0.430 to 2.400 μm). Its image swath width is 7.6 km, with a 30 meter resolution at 705 km altitude [17].

Figure 8. A Hyperion image of 242 bands (red 752.97 nm, green 651.28 nm, blue 447.89 nm).

C. IMAGE DISTORTIONS IN HYPERSPECTRAL REMOTE SENSING DATA

Hyperspectral image data are collected by sensors on aircraft or satellites mainly in digital format. Interpretation and analysis of these data requires digital processing as explained in the simplified block diagram of hyperspectral remote sensing imagery (Figure 5). These image data contain errors that can be classified into three categories: atmospheric, instrumental, and geometric distortions. This section describes the characteristics of image distortions that must be taken into account in processing hyperspectral image data.

1. Atmospheric Distortions

The atmosphere affects hyperspectral remote sensing data because of scattering and absorption, which attenuates the transmission of solar radiation. In the absence of an atmosphere, the solar radiance that can be measured by a sensor is provided by the formula:

$$L = E_{\Delta\lambda} * \cos\theta * \Delta\lambda * R / \pi \qquad (2.1)$$

where L is the radiance available for measurement, $E_{\Delta\lambda}$ is the average spectral irradiance in the band $\Delta\lambda$, R is surface reflectance and π accounts for the upper hemisphere of solid angle [2].

Using knowledge of the instrument response function, the radiance (L) can be obtained from the digital value representing the brightness of each pixel. Note that this formula is correct in the absence of an atmosphere, and does not take into consideration atmospheric effects. Solar radiation is affected by absorption and scattering caused by atmospheric molecules and aerosols. These particles are distinguished by their size relative to the wavelengths of visible light. Atmospheric molecules are smaller, while aerosols are larger than these wavelengths.

Absorption of solar energy by air molecules is a selective process which converts incoming energy into heat, a process that occurs at discrete wavelengths. For our purposes, water, ozone, oxygen, and carbon dioxide are the primary molecules that cause significant attenuation in electromagnetic radiation at the frequencies of interest. Figure 9 shows the spectral transmittance with respect to various atmospheric molecules, and shows the "atmospheric windows". Remote sensing systems are designed to operate in these regions called atmospheric windows, in order to minimize such attenuation. Nevertheless, compensation for radiometric distortion is still required.

Two different forms of scattering are typically defined: Rayleigh scattering which is caused by molecules, and Mie scattering which is caused by aerosols such us dust and industrial smokes. The effect of Rayleigh scattering decreases rapidly with wavelength

as the probability of scattering is inversely proportional to the fourth power of wavelength (~ λ^{-4}). By contrast, Mie scattering decreases less rapidly with wavelength. In addition, Mie scattering varies significantly depending on location, time, and environmental conditions.

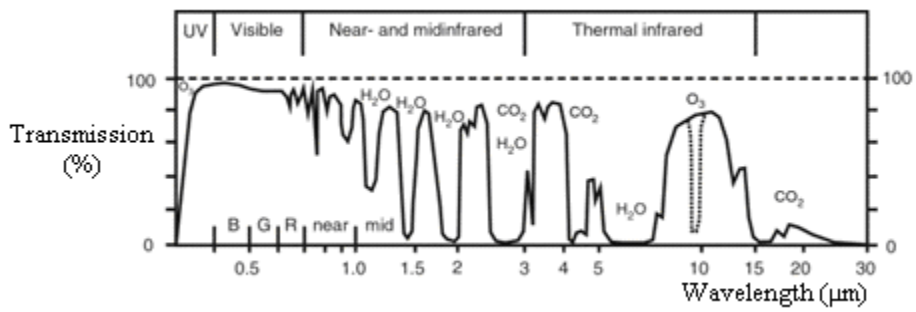

Figure 9. Characteristics of absorption by atmospheric molecules. [From 24]

The analysis of spectral imagery generally depends on an accurate compensation for the effects of the atmosphere, particularly absorption. In particular, narrow absorption bands have a significant influence on the measured radiance in specific bands (e.g. the water feature at 1130 nm). Aerosol scattering can be difficult to deal with, at least in part, because of its strong dependence on location and environmental conditions, such us humidity and temperature. Scattering is dominant at shorter wavelengths and instead of energy conversion, a change of path direction occurs, which depends on the aerosol size and the direction of incident light.

The atmospheric attenuation in the path from the ground to the sensor is dependant on the flight altitude of the platform and the sensor's field-of-view (FOV). Typically, a large FOV and a low-flying altitude cause the path length of the up-welling to change radically as a function of the pixel across the track [14].

The correction of atmospheric effects is called atmospheric calibration. The modeling approach for atmospheric calibration of hyperspectral images often makes use of the image data themselves [18]. There are several calibration models for hyperspectral images. Atmosphere Removal (ATREM) [19] is one of the most commonly used

models. It takes into account the altitude of the acquisition aircraft and differences in attenuation due to water vapor as a function of path length, but it does not take into account the pixel-based variation in attenuation due to the scattering component [14].

2. Instrumental Distortions

The main sources of instrumental errors are due to sensor calibration and scanner construction and must be taken into account by calibration. Sensor calibration is required because of radiometric errors that result in incorrect brightness values for the pixels in an image. The false measurements can be either in a spectral band or within the spectrum of a given pixel. The radiometric calibration of a sensor includes both the precision of the radiance measurement in appropriate units, typically power per area/solid angle/wavelength ($\mu W/cm^2/sr/nm$), as well as its conversion to a digital number.

Instrumental errors are mainly in the form of banding or striping. Banding is typically a visible noise pattern caused by memory effects. For example, after scanning past a bright target, such as snow, the detector's response is reduced due to memory effects. In the case of a uniform region extending beyond the bright target, recorded brightness values from the sensor will be slightly lower than corresponding values obtained on the following scan. Therefore, the scans in one direction will be darker than adjacent scans in the opposite direction (for a whisk-broom scanner). Striping is a line-to-line artifact phenomenon that appears in individual bands of radiometrically corrected data. Its source can be traced to individual detectors that are miscalibrated with respect to one another. In other words, striping is caused by problems in scan lines as scanning systems build up an image one line at a time.

The scanner's construction used in acquiring image data affects the type of noise that will be induced in the image. For example, variation in calibration between detector elements causes stripping along flight lines in a linear array scanner [20]. Additionally, improper spectral alignment between the entrance slit and the detector array induces noise in images collected by a linear scanner [21].

The accuracy of determining the surface reflectance depends on the sensor and its calibration. The spectral calibration is a function of the precision of the wavelength calibration and the spectral resolution of a given band. A precision to the nearest 0.1 nm

is necessary for an instrument with a 10 nm spectral resolution in order for the various absorption bands, such as that of water vapor, to be taken into account [21]. Focal plane sensors like that on HYDICE can have spectral "smile effects" – errors in wavelength which vary over the focal plane.

It is noteworthy that band to band instrumental errors are normally ignored in comparison to band to band errors from atmospheric effects. However, instrumental errors within a band can be quite severe and often require correction [2].

3. Geometric Distortions

Geometric distortions are quite significant when a remote sensing platform flies at low altitude and has a large FOV. In this case, pixels in the nadir line are smaller than pixels at the edges of the swath due to the panoramic effect [2]. The size of the pixel in a scan direction at scan angle θ is given by

$$p_\theta = \beta h \sec^2\theta = p \sec^2\theta \qquad (2.2)$$

where β is the instantaneous field of view (IFOV), h is the altitude, and p is the pixel direction at nadir. Assuming an aircraft flying at 1,500 m, with largest view angle 40°, and having a pixel size of 3 m at nadir, the size of the pixel at the edge of the swath will increase to approximately 3.4 m due to the panoramic effect. Additionally, geometric distortion occurs due to pixel displacement (dx) given by the formula

$$dx = dz \tan\theta / p_\theta \qquad (2.3)$$

where dz is the relative height over a reference elevation. Assuming a relative height of 20 m the pixel displacement will be 2.14 m.

Geometric errors are also found in scanner data and are induced by attitude and altitude variations of the aircraft, caused mainly by atmospheric turbulence and cross-winds. Figure 10 illustrates the changes of pixel geometry in an aircraft's attitude variations. For example, an increase in altitude will change the pixel's geometry as

illustrated in Figure 10.a. Also, a variation in the aircraft's velocity changes the pixel size along track (Figure 10.b). Finally, attitude variations in pitch, roll, and yaw cause along-track displacement, across-track displacement, and image rotation respectively.

Two techniques are used in reducing geometric distortions of aircraft scanner data. The first requires a good knowledge of the sources that induce errors in order to establish a correction formula. The second method does not require knowledge of the sources of distortion, but establishes a distortion model which transforms the image data to geographical space via a map.

4. Noise Modeling

Noise induced in an image can degrade the quality of the image to such a degree that important information is obscured. Therefore, noise removal should be the first step before information extraction from hyperspectral images. Noise removal can be achieved using image processing techniques. There are several different sources that induce noise in an image. However, from a mathematical point of view, noise in remote sensing hyperspectral images can be categorized into random and periodic noise.

Degradation in image quality is commonly caused by uncorrelated noise, the type of noise that image processing methods try to eliminate. In terms of a spatially-sampled image, uncorrelated noise is defined as the random grey level variations within

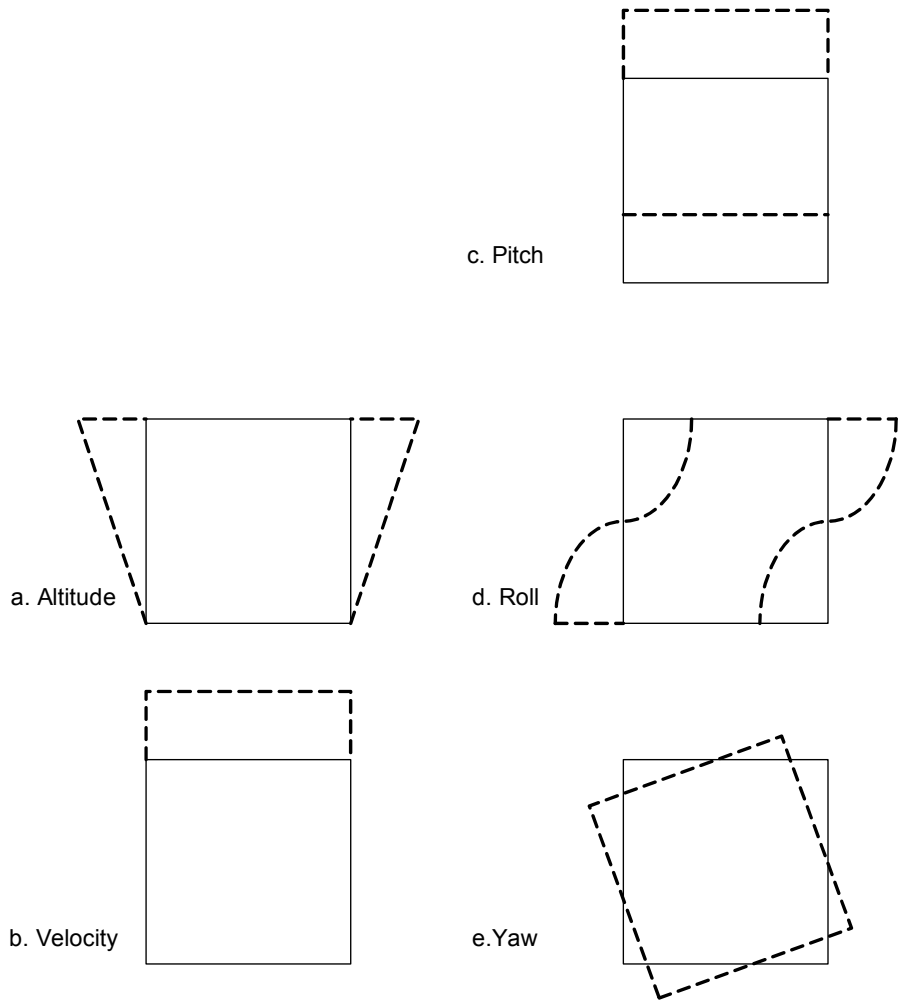

Figure 10. Effects of platform position and attitude errors on the region of earth being imaged, when these errors occur slowly compared with image acquisition [From 2].

an image that has no spatial dependence from pixel to pixel. This means the brightness of a pixel due to uncorrelated noise does not depend on the brightness of its neighboring pixels. From a mathematical point of view, the noise is characterized by its probability density function or histogram in the case of discrete noise.

The most common type of noise that appears in hyperspectral images -- and the one that we are most interested in -- is Gaussian noise. In most cases, the noise in an image can be modeled as the sum of many independent noise sources. This type of noise is represented as a normally distributed (Gaussian) zero-mean, random process with a probability destiny function f(x) given by

$$f(x) = \frac{e^{-(x-m)^2/2\sigma^2}}{\sqrt{2\pi}\sigma} \qquad (2.4)$$

where σ is the standard deviation of the noise and m is the mean. A histogram of Gaussian noise is shown in Figure 11. Data are distributed equally around their mean value. About 68% of the area under the curve is within one standard deviation of the mean, 95.5% within two standard deviations, and 99.7% within three standard deviations.

Assuming an image I, the effect of an additive noise process is the summation of the signal with the noise and is given for the ith and j^{th} pixel as follows

$$I(i, j) = S(i,j) + n_{ad}(i,j) \qquad (2.5)$$

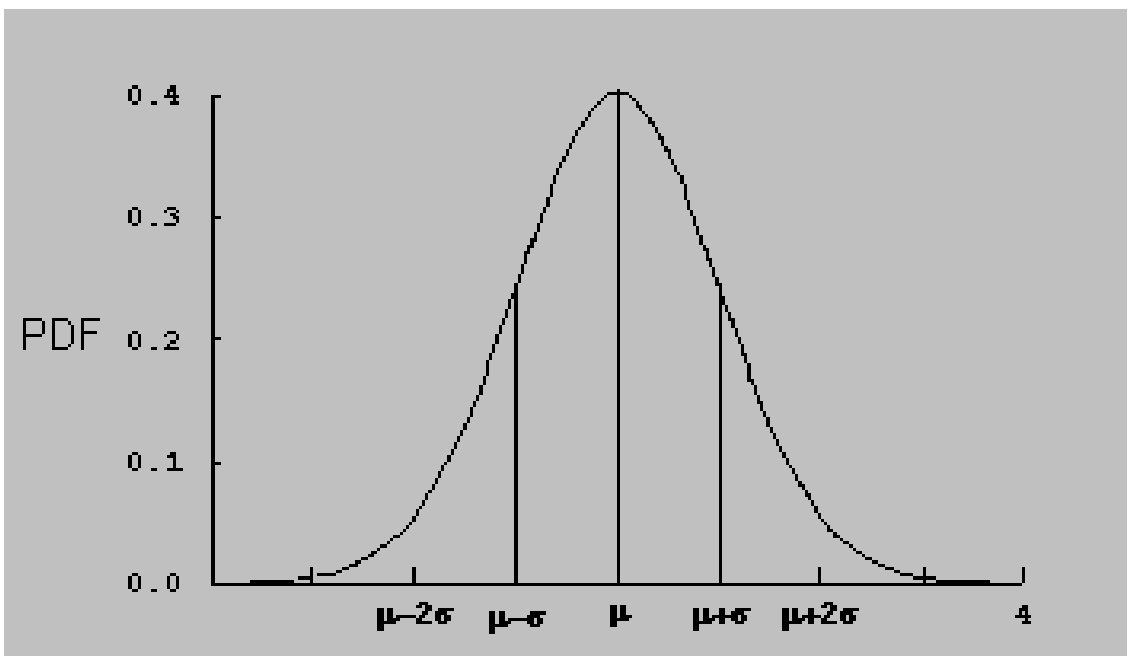

Figure 11. Histogram of a Gaussian noise function.

Another type of noise that commonly appears in hyperspectral images is periodic noise. This type of noise is caused by incorrect scan lines due to improper operation of systems and has the form of striping. Striping is measured by its offset and gain. Offset

is the addition or subtraction of a constant value to the recorded brightness values in an image, while gain is the multiplication of the data values by a factor. Striping is produced in image data by using a gain or offset factor for a given pixel that is incorrect, affecting one or more scan lines in the image. In periodic noise, the original data can be difficult to recover. Most signal processing methods try to detect the incorrect pixels and to replace them by a value based on neighboring pixels.

In this thesis we explore the ability of Principal Components Analysis (PCA) based techniques to eliminate Gaussian noise, as it is the noise that dominates in hyperspectral images. PCA is a versatile technique and is widely used for dimensionality reduction, data compression, and feature extraction. The applicability of PCA methods is investigated using AVIRIS, HYDICE and Hyperion image data.

III. PRINCIPAL COMPONENTS ANALYSIS

A. OVERVIEW

Multispectral and hyperspectral remote sensing image data consist of vector components arranged to form an image. These vector components or spectral bands do not contain completely independent information, but are usually correlated to some extent due to the spectral overlap of the sensors and the correlation in reflectance of materials at disparate wavelengths [1]. That means that variations in the brightness in one band may be mirrored by similar variations in another band (for example, when the brightness of a pixel in band 1 is high, it is also high in band 3). From a signal processing view, this correlation results in two undesirable effects. First, there is unnecessary redundancy which increases the data-processing cost without providing more information. Second, the data set includes both information and noise, and the noise content is relatively higher in these high-dimension data sets. Therefore, methods that capture the content in the original data, according to some criteria, are necessary. In remote sensing applications, the main criterion is to improve the image quality by reducing the dimensionality of the data and removing the noise.

Principal Components Analysis (PCA) is the most widely used linear-dimension method based on second order statistics. PCA is also known as the Karhunen-Loeve transform, singular value decomposition (SVD), empirical orthogonal function (EOF), and Hotteling transform. PCA is a mathematical procedure that facilitates the simplification of large data sets by transforming a number of correlated variables into a smaller number of uncorrelated variables called principal components. The basic applications of PCA, as applied to remote sensing, are data compression, from the reduction in the dimensionality of the data, and information extraction, by segregation of noise components. This is done by finding a new set of orthogonal axes that have their origin at the data mean and are rotated to a new coordinate system so that the spectral variability is maximized. Resulting PC bands are linear combinations of the original spectral bands and are uncorrelated.

In this chapter, two methods, that are included in the PCA family of techniques, are examined for image enhancement as applied to the field of target detection: the basic PCA and Maximum Noise Fraction (MNF) or Noise Adjusted Principal Components (NAPC) [11]. First the basic mathematics are explained and then the methods are implemented and results are discussed.

1. Basic Principal Components Analysis

This section discusses the mathematical background of the basic PCA. The basic PC operation is explained, for reasons of simplicity, using a two dimensional data set, since the plots are better understood and the mathematics are easier. In multispectral and hyperspectral remote sensing image data there are four to several hundred dimensions, but the basic principles are the same as in the two dimensional example, except that the computations become more complicated.

An image in remote sensing applications can be represented by a matrix with components that represent the measured intensity values of the pixels. Assuming that an image has n pixels, measured at k spectral bands, the matrix characterizing the image is as follows:

$$x = \begin{bmatrix} x_1 \\ : \\ x_k \end{bmatrix} \tag{3.1}$$

where $x_1, \ldots, x_k$ are vectors of n elements.

For the purpose of this explanation of PC, it is assumed that the matrix consists of 10 pixels measured at two bands. Therefore, two vectors, each having 10 components, represent the intensity values (reflectance) of each pixel in each band. In this example, the sample data set is the following 2×10 matrix:

$$x = \begin{bmatrix} 1.7 & 2.1 & 3.1 & 1.4 & 0.7 & 1.4 & 2.3 & 2.1 & 1.1 & 1.6 \\ 1.8 & 2.4 & 2.9 & 1.2 & 0.8 & 2.1 & 2.7 & 1.9 & 1.3 & 1.7 \end{bmatrix}$$

Additionally, the position of each pixel is plotted in a two-dimensional spectral space in which each axis represents reflectance in the band indicated (Figure 12). This scatter plot illustrates the degree of correlation between the two variables and indicates a high correlation between the image pixels in the two bands. From a signal processing view, the majority of the information about two highly correlated variables can be captured by a regression line, which represents the best fit of the linear relationship between the variables. One way of viewing the PCA is that the goal is to linearly transform the data so that it approximates that regression line.

Several steps are involved in this procedure. The first step in the PC procedure is generally the subtraction of the mean from each of the data dimensions. The mean spectrum vector represents the average brightness value of the image in each band and it is defined by the expected value as follows:

$$m = \frac{1}{\mathrm{N}} \sum_{j=1}^{N} x_j = \begin{bmatrix} \mathrm{m_1} \\ \vdots \\ \mathrm{m_k} \end{bmatrix} \tag{3.2}$$

where m is the mean spectrum vector, N is the total number of image pixels, and x_j is a vector representing the brightness of the jth pixel of the image. Therefore, the components of the mean spectrum vector m represent the average brightness of the image in each band. The mean spectrum vector of the sample data is shown in Figure 12(a).

By subtracting the mean of the data, the mean spectrum is zero in each band. This is called a mean shift. The PC analysis decorrelates the data mainly by rotating the original axes, and therefore, the mean shift does not change the attributes of the resulting PC images. The only difference is an addition of a constant value in each band. This makes the decorrelation more evident in subsequent stages, but is not necessary. The mean-correction results in data centered about the axes origin, and therefore, negative

values appear in the pixel coordinates. This can be disorienting in remote sensing applications, and some software packages add back a positive offset after the decorrelation step [3].

The second step in the PC method is to calculate the covariance matrix, which is a square symmetric matrix, where the diagonal elements are variances and the off-diagonal elements are covariances. From a spectral imagery point of view, the variances represent the brightness of each band and the covariances represent the degree of brightness variation between bands in the image. Additionally, covariances that are large compared to the corresponding variances in a spectral pair indicate high correlation between these bands while covariances close to zero indicate little correlation in these spectral pairs [2].

The covariance matrix is computed by the following formula

$$\sum_x = E\left\{(x - m)(x - m)^T\right\} \tag{3.3}$$

where m is the mean spectrum vector of the image and x is the vector representing the brightness values of each pixel. For the sample data set given above, the 2×2 covariance matrix is given by

$$\sum_x = \begin{bmatrix} 0.4628 & 0.4133 \\ 0.4133 & 0.4484 \end{bmatrix}$$

Note that the correlation matrix is frequently used in lieu of the covariance matrix. This changes the relative weighting of the channels (bands) in the decorrelation transform, but is conceptually the same. The correlation matrix is as follows

$$\sum_x = \begin{bmatrix} 1.0000 & 0.9073 \\ 0.9073 & 1.0000 \end{bmatrix}$$

The next step in the PCA analysis is the calculation of the eigenvectors and eigenvalues of the covariance matrix. The eigenvalues $\lambda = \{\lambda_1 \ldots \lambda_k\}$ of a k×k square matrix are its scalar roots, and are given by the solution of the characteristic equation

$$| \Sigma_x - \lambda \mathbf{I} | = 0 \tag{3.4}$$

where **I** is the identity matrix. The eigenvectors are closely related with the eigenvalues and each one is associated with one eigenvalue. Their length is equal to one and they satisfy the equation

$$\mathbf{\Sigma}_x \, \mathbf{v}_k = \lambda_k \, \mathbf{v}_k \qquad (3.5)$$

where $\mathbf{v}_k$ is the eigenvector corresponding to the λ_k eigenvalue and its dimension is $1 \times k$. Applying these above mentioned formulas with the covariance matrix of the sample data results in

$$\lambda = [0.0422 \quad 0.8690] \qquad \text{and,} \qquad v = \begin{bmatrix} 0.7010 & -0.7132 \\ -0.7132 & -0.7010 \end{bmatrix}$$

Figure 12(b) presents the normalized data (mean-corrected) in the two dimensional example, where both eigenvectors have been plotted on top of the data.

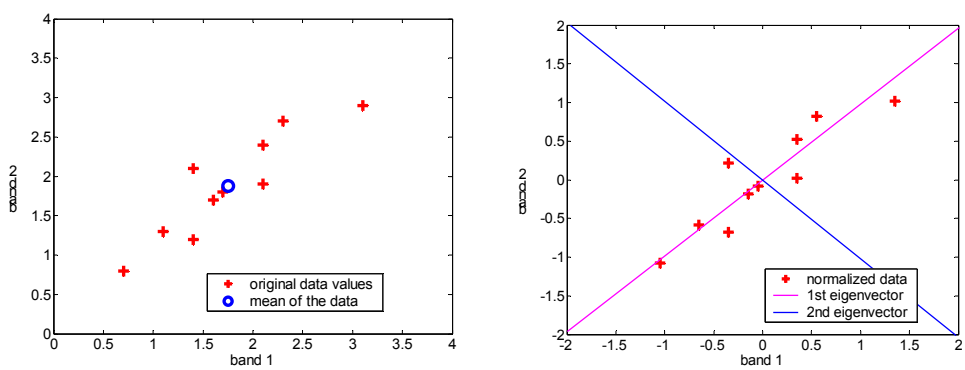

Figure 12. Data in a PC example (a) original data and their means (b) normalized data with the eigenvectors of the covariance matrix overlaid.

The eigenvectors are orthogonal to each other and provide us with information about the patterns of the data. The first eigenvector provides a line that approximates the regression line of the data – this axis is defined by maximizing the variance on this line. Therefore, the second eigenvector provides a line that is orthogonal to the first, and contains the variance that is away from the primary vector. In the case of three variables, a space will be used instead of a plane as in the two-dimensional example. Then, a "regression" plane can be defined for the data that maximizes the variance. When more

than 3 variables are involved, the principles of maximizing the variance are the same but graphical representation is almost impossible.

The fourth step in the PC analysis is the determination of the components that can be ignored. An important property of the eigenvalue decomposition is that the total variance is equal to the sum of the eigenvalues of the covariance matrix, as each eigenvalue is the variance corresponding to the associated eigenvector. The PC process orders the new data space such that the bands are ordered by variance, from highest to lowest. The eigenvector with the highest eigenvalue is the first principal component (PC) and accounts for most of the variation in an image. The second PC has the second larger variance being orthogonal to the first PC, and so on.

A transformed data set is created by using the eigenvectors from the diagonalization of the covariance (or correlation) matrix. After selecting the eigenvectors that should be retained, the following formula is applied:

$$\text{(Final Data Set)} = \text{(Eigenvectors Adjusted)'} \times \text{(Data Adjusted)'} \qquad (3.6)$$

where (Eigenvectors Adjusted)' is the matrix of eigenvectors transposed so that the eigenvectors are in the rows with the first eigenvector on the top and (Data Adjusted)' is the matrix with the mean-corrected data transposed.

In the provided example, in which a two dimensional data set was used, the choices are simply two: to keep both eigenvectors or to ignore the less significant eigenvector, the one with the smaller variance. By keeping both eigenvectors, there is no loss of information, and the final data set is depicted in Figure 13(a), showing the original data set rotated. The alternative is illustrated in Figure 13 (b), where only the most significant eigenvector, the one with the largest eigenvalue is kept. This results in a single dimension vector with components along the new x-axis. In this case, dimensional reduction using PCA has occurred by removing the contribution of the less significant eigenvector. This rather trivial example illustrates the case where multi-dimensional

imagery has been reduced to a single band – some sort of average brightness image, not unlike that which would have been obtained by a panchromatic sensor.

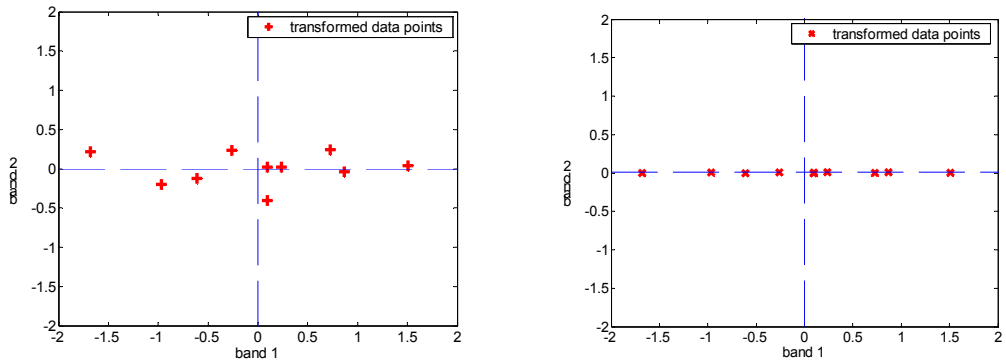

Figure 13. (a) Derived data set using both components (b) Derived data set using only one component.

Dimension reduction in multivariate data it is not an easy task and many methods have been proposed. The main goal of these methods is to find the intrinsic dimensionality of the data set – that is the minimum number of free variables needed to model the data without loss [4]. Typically, four methods for reducing the dimensionality of multispectral and hyperspectral image data are implemented in remote sensing applications.

The first and most common approach is the scree test introduced by Cattell in 1966 [5]. It is a graphical method in which the eigenvalues are plotted in a single line plot versus the PC number. This plot shows which of the initial principal components accounts for most of the variance in the scene. The eigenvalue plot typically shows a sharp drop from a high initial value, then a bend in the curve, extending then into a fairly level tail. It is assumed that the variance elements represented in the tail of the curve represent only the random variability in the data, meaning the noise components and mainly instrumentation noise. Therefore, according to the scree test, the components to the left of the break, or knee in the curve, should be retained. A typical eigenvalue plot is shown in Figure 14.

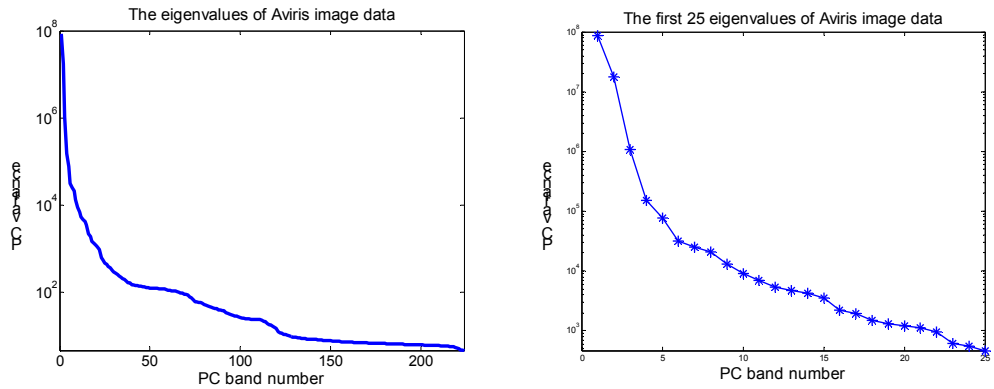

Figure 14. Eigenvalue plots of the AVIRIS image.

Another method for determining the intrinsic dimension of the data is the Kaiser criterion [6]. In this case, the correlation matrix is used, transform bands are evaluated, and those with a variance greater than or equal to one are retained. Transform bands with a variance greater than or equal to one contain at least as much information as the original.

The third approach to dimension reduction was proposed by Yury [7]. Continuous Significant Dimensionality (CSD) is defined by the formula,

$$CSD = \sum_{j=1}^{k} \min(\lambda_j, 1) \qquad (3.7)$$

where λ_1, λ_2, ... λ_k are the eigenvalues of the correlation matrix. The CSD value indicates the number of PC components that should be retained.

Cumulative variability is the fourth common method for dimensionality reduction. The criterion here is that the first components that account for at least 90% of the total variability are retained. It is estimated that these components capture the useful information of the scene.

The above methods work when there are clearly only relatively few PC bands, as with the synthetic data. However, real hyperspectral data can give quite different results due to the ill-conditioning of the dimension estimation problem [4]. In section (B.1) all

the above mentioned methods for dimension reduction are investigated for their effectiveness on hyperspectral image data.

2. Minimum Noise Fraction Transform

The minimum (or maximum) noise fraction (MNF) is a second major algorithm belonging to the family of PCA techniques. It was developed by Green, Berman, Switzer, and Graig in 1988 as a method that takes into account sensor noise. By contrast, the basic PCA procedure takes into consideration only the variances of each PC component and assumes that noise is already effectively isotropic. However, real sensor noise is typically not isotropic, or "white". In addition, the variances of noise components can be higher than the variances of components that represent the local information of the scene. Therefore, PCs do not always produce images of decreasing image quality, even though the variance is declining monotonically with PC number. It is not unusual to find, that in noisy images, local information can be represented in higher PC components. A measure of image quality is the signal-to–noise ratio (SNR). The MNF transform orders the images in terms of this metric, thus ordering them based on image quality.

The MNF transform is effectively an algorithm consisting of two consecutive Principal Component's transformations. The application of this transformation requires knowledge of an estimate of the signal and noise covariance matrices. The first transform is derived from the covariance matrix for the sensor noise, and is designed to decorrelate and whiten the data with respect to the noise. The main difficulty with this process is obtaining a proper estimate of the sensor noise. Several methods have been suggested: (1) simple differencing, in which the noise is estimated by differencing the image between adjacent pixels (2) casual simultaneous autoregressive (SAR), in which the noise is estimated by the residual in a SAR model based on the W, NW, E and NE pixels (3) differencing with the local mean (4) differencing with the local median, an alternative to the local mean method in order to avoid blur edges and (5) quadratic surface, in which the noise is estimated as a residual from a fitted quadratic surface in a neighborhood.

As noted, the MNF transform contains two PC transforms. The first transformation, based on an estimated noise covariance matrix, results in transformed data for which the noise is uncorrelated with unit variance. The second transformation is a basic PCA on the noise-whitened data. Then, both the eigenvalues and the corresponding images, which are called eigenimages, are examined in order for useful information to be separated from noise. Generally, eigenimages associated with large eigenvalues consist of useful information while eigenvalues close to one indicate noise-dominated data. By discarding the components with small eigenvalues, the noise is separated from the data and the inherent dimensionality of the image is determined.

Additionally, this method is used for spatial smoothing in which a spatial filter is applied to the noise images, and the filtered data are transformed back to the original data space using an inverse MNF transform.

The main characteristic of the MNF transform is that it orders the component images based on image quality by measuring the SNR. Therefore, it is invariant to scale changes, in any band, because it depends on the SNR instead of variance, like basic PCA, to order the component images [8]. This transformation is also called the Noise Adjusted Principal Components transform because it is equivalent to sequentially transforming the data to a coordinate system in which the noise covariance matrix is the identity matrix followed by a PC transformation.

B. APPLICATION OF PCA TECHNIQUES

The basic algebra behind PCA techniques has been explained in the previous sections using a two-dimensional data set focusing on the statistical interpretation in the context of remote sensing applications. In this section, two PCA techniques, the basic PCA and MNF transformation, are implemented on three different image data sets. The objective is to examine the theory to investigate the efficiency of these techniques for various remote sensing tasks.

Data from AVIRIS, HYDICE and Hyperion are used to explore the PCA techniques of interest. The tool used for this work is the product ENVI (Environment for Visualizing Images) software, version 3.5, produced by Research Systems Inc. The characteristics of these data were presented in Chapter II. As a reminder, each covers the

0.4-2.5 μm spectral range. The AVIRIS, HYDICE and Hyperion sensors have 224, 210 and 242 bands, respectively. The Hyperion sensor, mounted on the EO-1 satellite, provides imagery measured from an altitude of 705 km. The other two provide airborne imagery.

In subsequent sections, methods of determining the intrinsic dimensionality of spectral data sets are explored, and the most appropriate approach is implemented. PCA techniques are investigated using the statistics of correlation and covariance matrices. Also, the resulting images from the basic PCA and MNF transforms are presented and their contribution to information extraction is discussed.

1. Determining the Intrinsic Dimension of Data

In this section, the methods for determining the intrinsic dimension of data are investigated for their effectiveness in hyperspectral data sets. The correlation matrix is first computed and then the eigenvalues are derived. The summation of the eigenvalues is equal to the total number of bands (e.g. if the number of bands is 224 the summation of all eigenvalues is 224) because the elements of the main diagonal in the correlation matrix are all equal to one. Figure 15 shows the 25 first eigenvalues of the correlation matrix for each image in a scree graph and Table 1 lists the percentage of cumulative variability of the 20 first eigenvalues.

Based on the scree test criterion for the AVIRIS image, 4 PCs are retained, since the curve flattens after these 4 components. Using the same methodology, 3 components of the HYDICE and 2 of the Hyperion images are retained. The cumulative variance criterion, in which a total variance of at least 90% is required (shown in Table 2) yields 3, 2, and 14 retained components for AVIRIS, HYDICE, and Hyperion images, respectively. By comparison, the Kaiser criterion gives higher values, with 5, 5, and 16 bands retained. Finally, the CSD values are calculated and are 13.16, 7.39, and 33.7 for the AVIRIS, HYDICE, and Hyperion images, respectively, and correspond to 14, 8, and 34 retained PCs. Table 3 summarizes the results for the three methods.

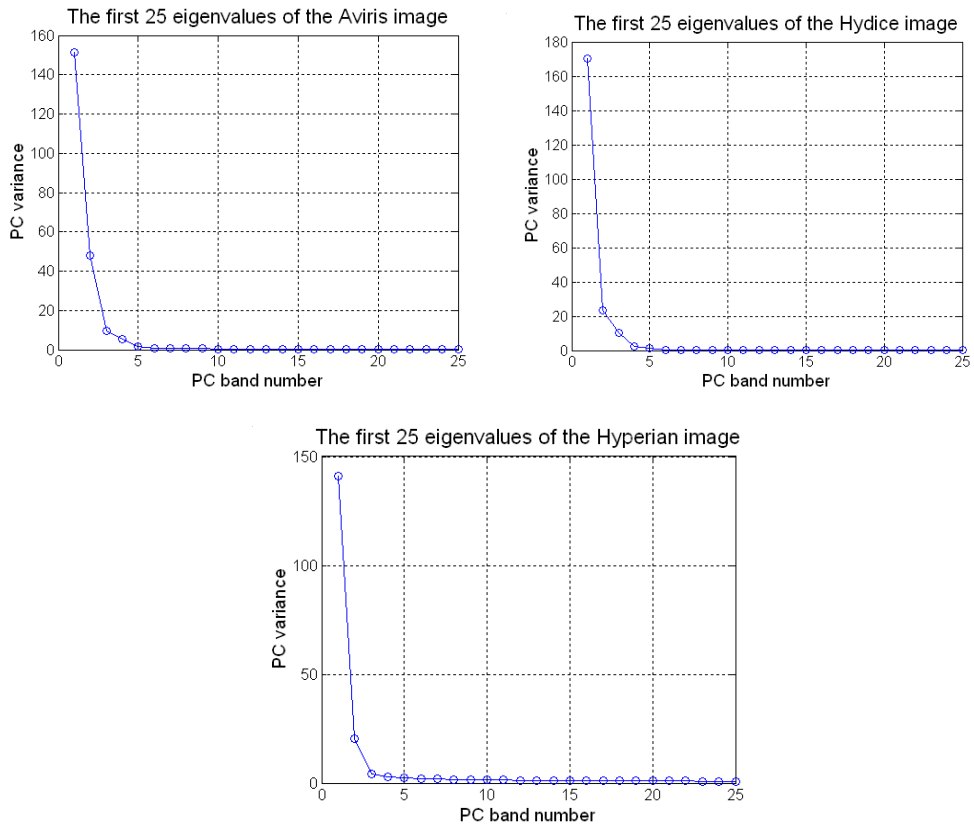

Figure 15. Scree graph of the first 25 eigenvalues of the correlation matrix for the AVIRIS, HYDICE, and Hyperion images.

Table 3 shows that the cumulative variance criterion, the scree test, and the Kaiser criterion give approximately the same result (retain 3-5 components) for the AVIRIS and the HYDICE images. In contrast, the Hyperion image, the Kaiser and cumulative variance criteria require retention of a similar number of components (14 and 16), while the scree test requires only 2 components. The CSD technique indicates, in all three cases, that more components are required: 14, 8, and 34, respectively. It is noted that Hyperion images are generally noisier than AVIRIS or HYDICE images and this is probably the reason for different results among the scree test and the Kaiser and cumulative variance criteria, for this image. Therefore, the methods for determining the intrinsic dimensionality of the data seem to yield quite different results with hyperspectral images, especially when data are noisy. The next part of the analysis is visual inspection of the PC images to allow for better estimation and determination of the components that include useful information.

PC number	AVIRIS image		HYDICE image		Hyperian image	
	Eigenval.	% cumulative	Eigenval.	% cumulative	Eigenval.	% cumulative
1	151.48	67.63	170.19	81.05	140.90	69.07
2	47.85	88.99	23.41	92.20	20.50	79.13
3	9.60	93.28	10.25	97.08	4.16	81.17
4	5.22	95.61	2.31	98.18	2.77	82.53
5	1.67	96.36	1.42	98.86	2.32	83.67
6	0.78	96.71	0.45	99.08	2.05	84.67
7	0.63	96.99	0.39	99.27	1.80	85.56
8	0.55	97.24	0.14	99.33	1.72	86.40
9	0.52	97.47	0.13	99.40	1.58	87.18
10	0.46	97.68	0.13	99.46	1.36	87.85
11	0.43	97.88	0.11	99.51	1.32	89.13
12	0.38	98.05	0.10	99.56	1.28	89.73
13	0.36	98.21	0.09	99.61	1.22	90.31
14	0.35	98.37	0.08	99.65	1.17	90.82
15	0.34	98.52	0.08	99.69	1.03	91.31
16	0.31	98.66	0.07	99.72	1.01	91.80
17	0.30	98.80	0.06	99.76	0.99	92.28
18	0.29	98.93	0.06	99.79	0.98	92.75
19	0.27	99.05	0.05	99.82	0.96	93.22
20	0.26	99.17	0.03	99.83	0.95	93.67

Table 1. Eigenvalues and cumulative percentage of the correlation matrix for AVIRIS, HYDICE, and Hyperion images.

Criterion	AVIRIS image	HYDICE image	Hyperion image
Cumulative variance	3	2	14
Scree test	4	3	2
Kaiser test	5	5	16
CSD	14	8	34

Table 2. Intrinsic dimension (retained PC's) for AVIRIS, HYDICE, and Hyperion images for all methods.

Figure 16 shows the PC images for the 3 sensors. And by observing these images, it can be seen that the scree test gives a good indication, in all cases, of the

number of components that should be kept when both dimension reduction and information extraction must be achieved. However, by keeping only three components in the AVIRIS data (although a large fraction of the information is retained) it is possible that local information may be lost, as the 14th PC is still without much noise.

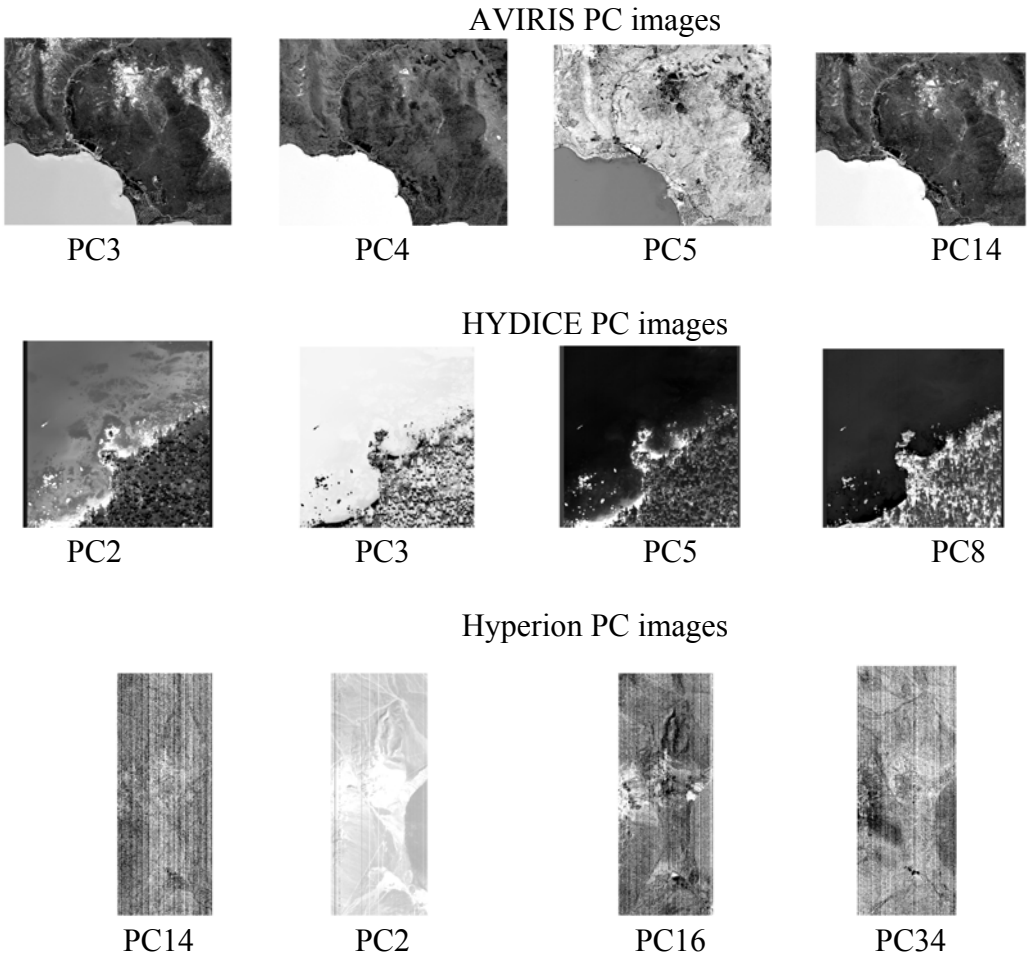

Figure 16. Principal component images for AVIRIS, HYDICE, and Hyperion data using the correlation matrix corresponding to the PCs that should be retained based on different methods.

Several experiments were conducted using the MNF transform on these same images, and results were similar, regarding the determination of the intrinsic dimension of the data. As in the PC transform, the scree test works well, but visual observation of the component images is necessary. Therefore, for the rest of this thesis the scree test and visual inspection of the component images will be used for determining the intrinsic dimensionality of the data.

2. Basic Principal Components Analysis

In remote sensing applications the spectral bands are highly correlated due to the wide frequency range of the energy reflected from the ground and the nature of reflective materials. A scatter plot between two bands is a common method of representing correlated bands. Figure 17 shows the scatter plot between a pair of bands for the original AVIRIS and HYDICE image data. It is obvious that the positions of the pixels in both plots approximately resemble a line. This indicates that these bands are highly correlated and, therefore, data are redundant. Similar scatter plots, indicating redundant data, exist for most of the band pairs. The purpose of the basic PCA is to produce a data space in which the bands are uncorrelated. By retaining a few components the representation of the image data can be more efficient and effective.

In sequence, the PC transform will be applied to each of the sensors. The AVIRIS sensor, considered to have the lowest number of sensor artifacts and the best SNR, will be studied first.

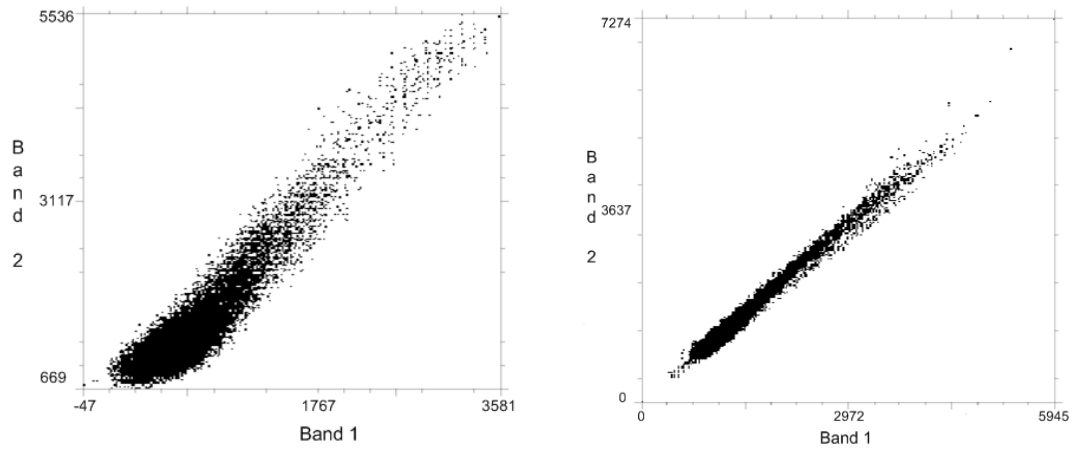

Figure 17. Scatter plots of original image data (a) AVIRIS band 1 versus band 2 and, (b) HYDICE band 1 versus band 2.

A PC transform is applied to the AVIRIS data. The covariance matrix is used for computation of the eigenvectors and eigenvalues. Figure 18(a) shows the eigenvalue of each PC and 18(b) shows a detailed view of the first 25 eigenvalues. Note that the y-axis

of the plots is logarithmic. Also, Table 3 presents more information about the statistics related to the first 25 eigenvalues. The first 24 PC images are depicted in Figure 20.

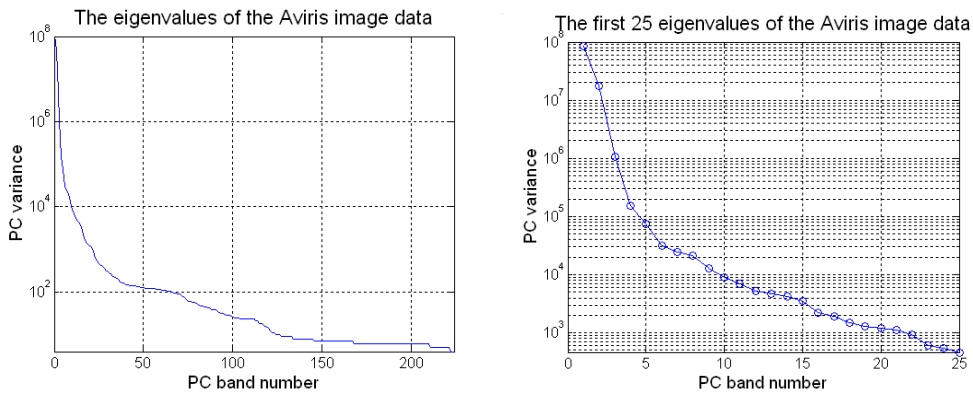

Figure 18. Scree graph for AVIRIS data using the covariance matrix (a) 224 eigenvalues and, (b) the first 25 eigenvalues (y-axis is logarithmic).

The scree graph of the eigenvalues of the covariance matrix (Figure 18) indicates that 3 or 4 components contain most of the useful information as the slope of the curve has a smooth decrease after the 3rd eigenvalue. Keeping that in mind, the PC images are examined for determination of the intrinsic dimensionality of the AVIRIS image data.

The first PC band contains the largest percentage of data variance, and it is usually dominated by topography (illumination). The image corresponding to the first PC resembles an aerial photograph and represents the scene average brightness. The second PC band contains the second largest data variance, and each successive PC accounts for a progressively smaller proportion of variation in the original data. By observing the second PC image, it is obvious that there is additional information content. In this water scene, this component reflects variations in water depth. High values in the second PC indicate shallow areas and decreasing brightness values depict increasing water depth. The populated area near the lake is also more recognizable and the hills are more clearly distinguishable. The third PC image is similar to the second, but generally reveals more detail. The vegetation on the land is distinguished better, while variations in water depth, hills, and the populated area are still well represented. Therefore, each of the first PC components is mainly associated with one type of material.

Beyond the first 3 components, subsequent PC images do not appear to provide any additional useful information. Therefore, based on both the scree test and visual inspection of the PC images, the third PC image completes the most efficient and informative representation of the data and it represents the intrinsic dimensionality of the image. The cumulative variance of the 3rd PC image is 99.64% and this indicates that the rest of the PC bands contain the least correlated information - typically noise in the original data.

Generally, the remaining PC images shown in Figure 19 do not provide any additional information about the scene. However, a few points are noticeable. In the 5th and 6th PC images areas well-defined in previous component images, are not distinguishable any more. Band 7 is very noisy, and shows horizontal strips which appear to be instrument artifacts. Higher order bands (8 and 9) again seem to provide information content. Band 10 is also noisy and generally all bands above 10 appear noisy, because they exhibit very little variance due to noise in the original data.

This scene (Figure 19) illustrates a frequent characteristic of the output from PC transforms – the PCA, in this case, does not provide images of monotonically decreasing quality. It is possible that useful information is included in bands 8 and 9. This is because basic PCA assumes no *a priori* knowledge of the scene, and it concerns itself only with variances of the decorrelated data. Figure 20 depicts the decorrelation of the data produced by the PCA transform by showing the scatter plots for PC bands 1 versus 2 and PC bands 2 versus 3. The data are clearly uncorrelated.

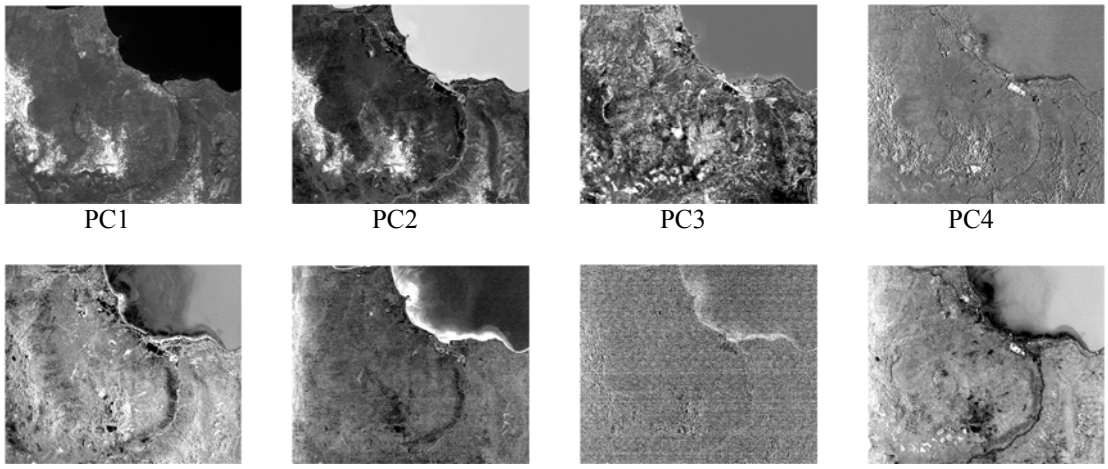

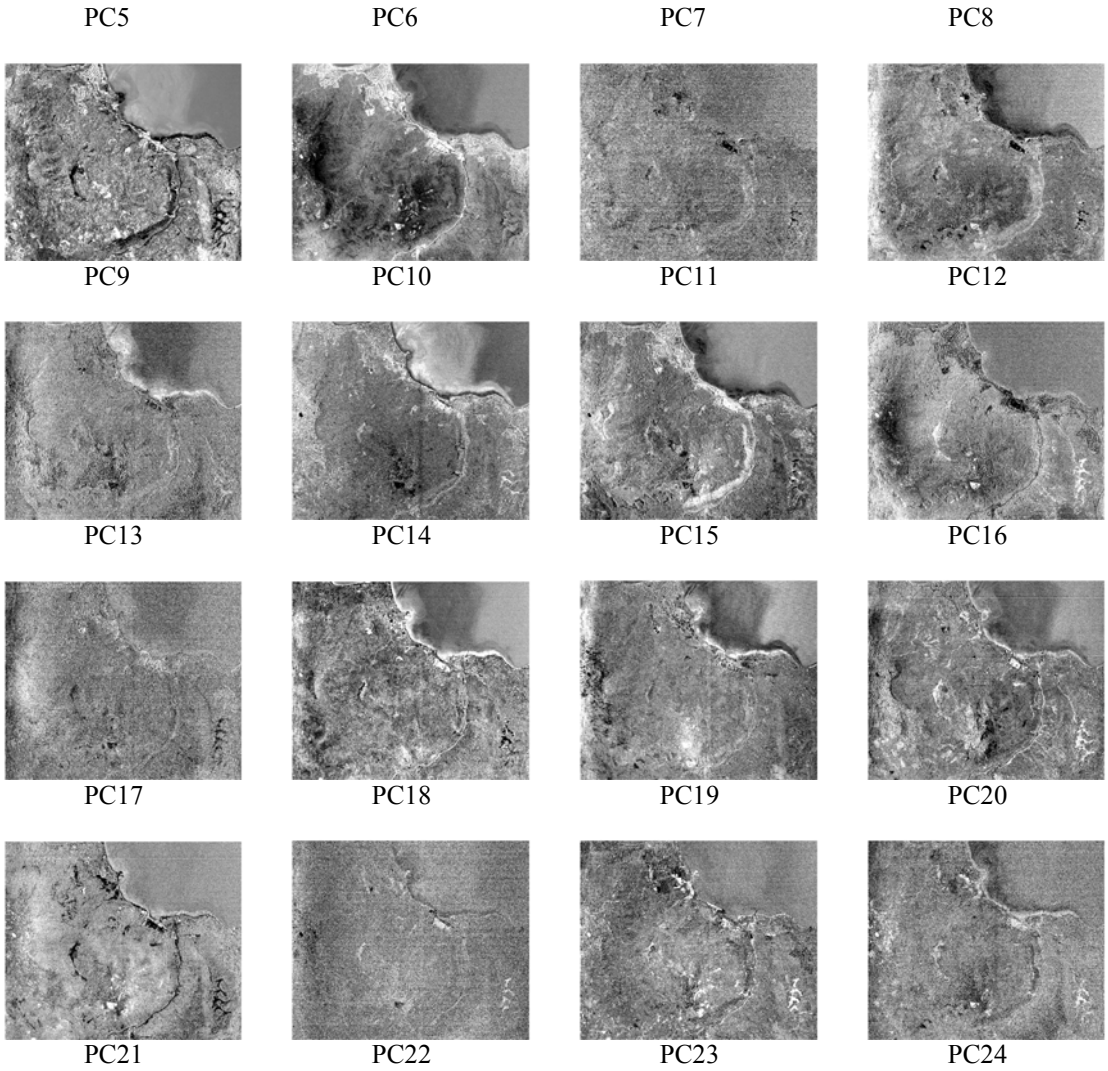

Figure 19. First 24 PC images of AVIRIS image data.

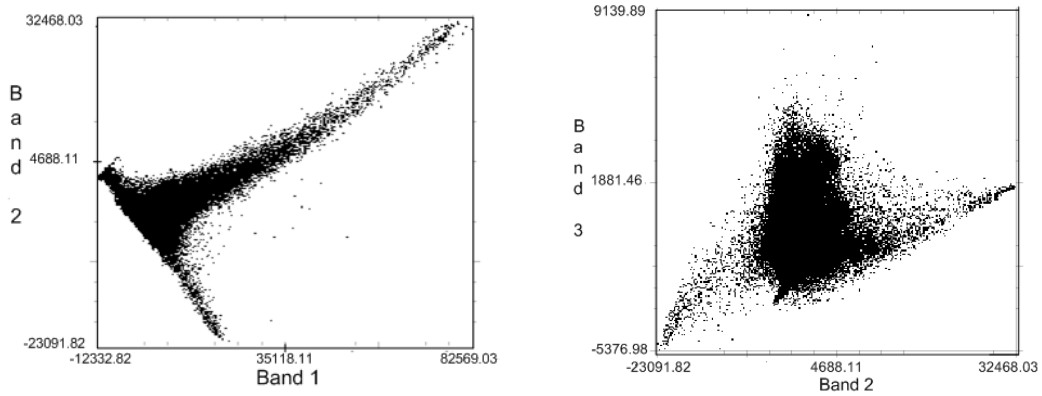

Figure 20. Scatter plots of PC bands of AVIRIS image data (a) band 1 versus band 2 and, (b) band 2 versus band 3.

The same procedure is followed for the HYDICE scene. A forward PC transformation is applied to the data using the covariance matrix and, as in the AVIRIS image, the scree graph of the eigenvalues is plotted and is shown in Figure 21, with details given in Table 3, and the first 24 PC images given in Figure 22.

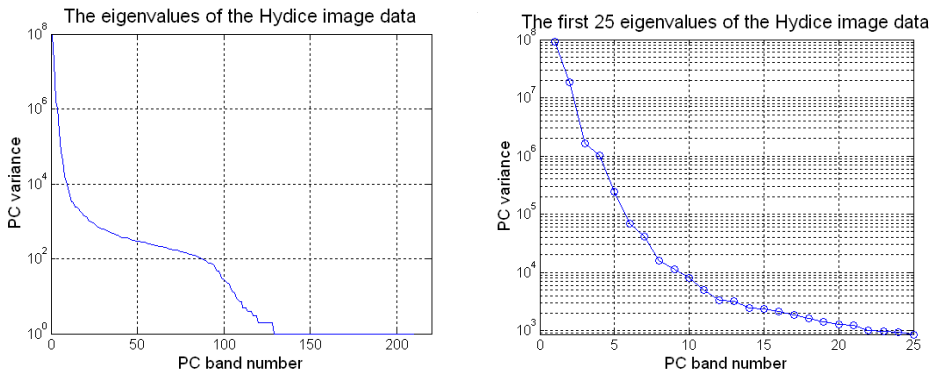

Figure 21. Scree graph for HYDICE data using the covariance matrix (a) 220 eigenvalues and, (b) the first 25 eigenvalues (y-axis is logarithmic).

The determination of the intrinsic dimension of the data is not clear in the scree graph, because there are two points at which the slope drops, after the third and the seventh eigenvalue. However, a visual inspection of the transformed images gives results similar to those found with the AVIRIS data. The first component appears as a black and white (monochrome) photograph of the scene; and the second PC image represents water depth variations. The fourth PC image largely completes the representation of the scene,

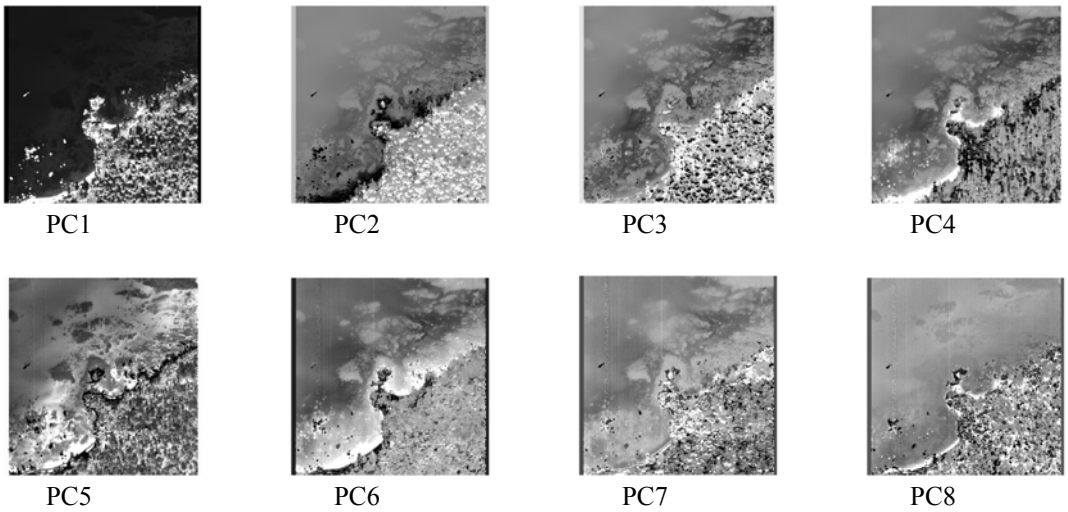

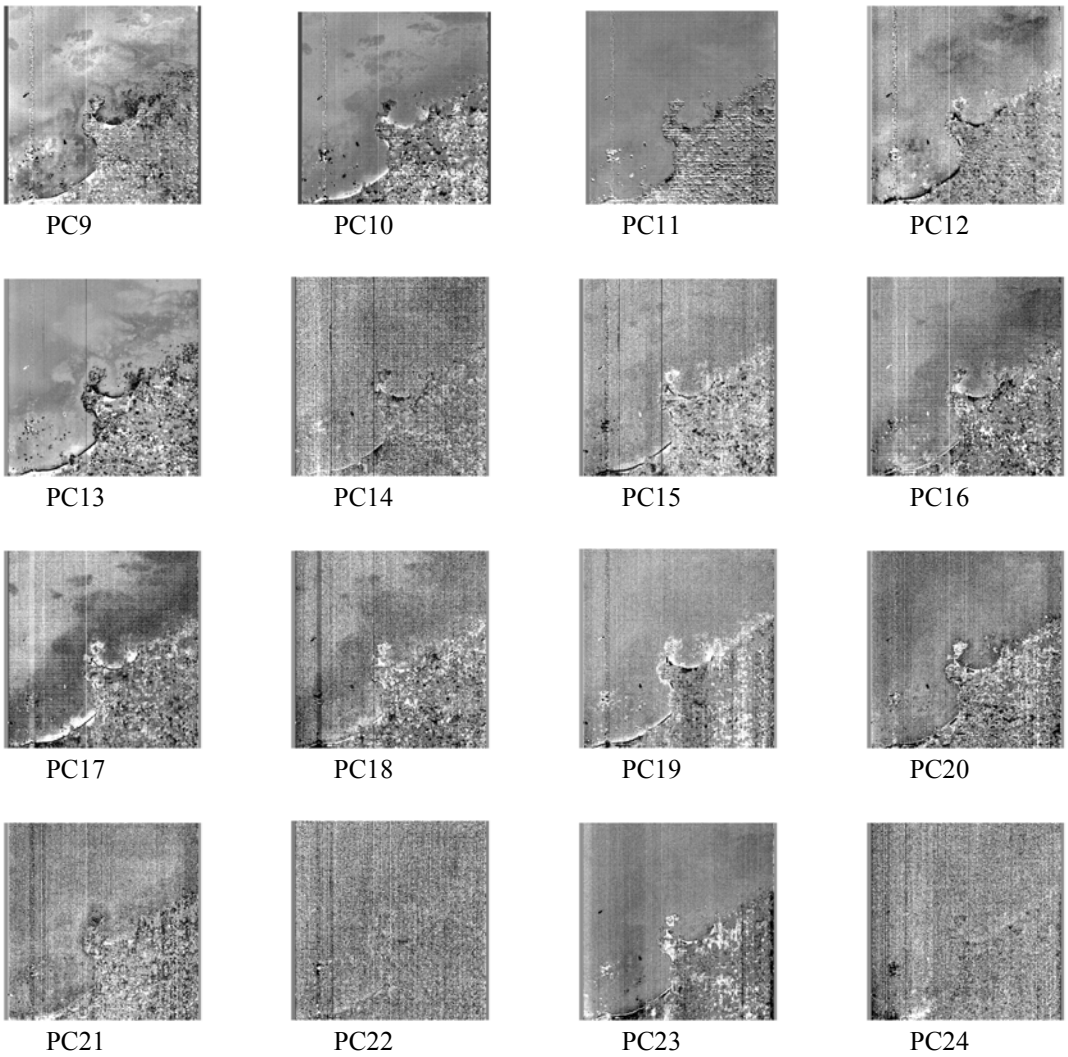

Figure 22. First 24 PC images of HYDICE image data.

bringing the total variability up to 99.61% of the total image variability. The transform images start to become noisy from band 5 on, as vertical strips appear on the left side of the image. Higher PC images contain increasingly more noise and almost no additional information, as represented in PC images higher than 14. The PC images indicate that HYDICE data contain more noise than AVIRIS data for these scenes.

The procedure is repeated for Hyperion data. Again, the eigenvalues of the covariance matrix are plotted in Figure 23, additional information is shown in Table 3,

and the first 24 PC images are presented in Figure 24. There are significantly more artifacts in Hyperion data, at least in part due to calibration issues (gains and offsets, bad pixels).

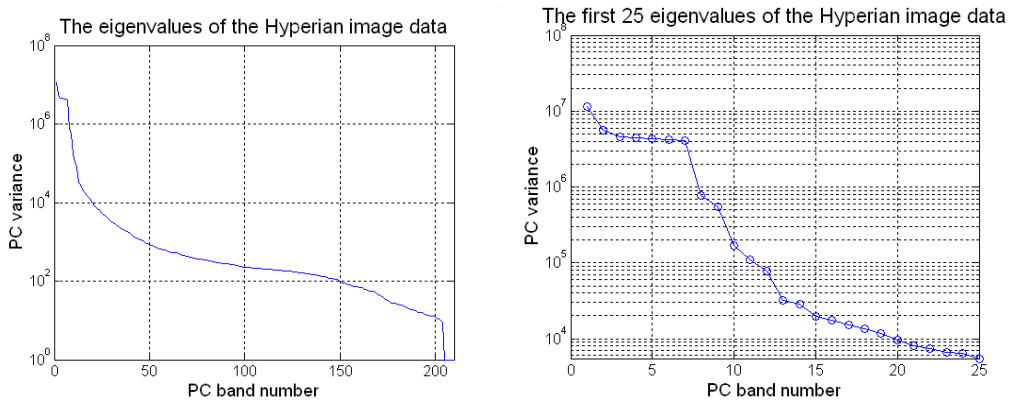

Figure 23. Scree graph for Hyperion data using the covariance matrix (a) 210 eigenvalues and, (b) the first 25 eigenvalues (y-axis is logarithmic).

In the scree graph there are two significant abrupt changes in the curve, as with the HYDICE data, indicating the cutoff points for determination of the retained components. These are the second and tenth eigenvalues. From observing the PC images, it is obvious that the image data is very noisy, as vertical lines begin to appear even for the first PC image. This is mainly instrumental noise. With the exception of the tenth PC image, which is a good representation of the overall scene, the images above PC 2 do not provide significant information about the scene, as they contain much noise. Of note is that the information distribution is quite different from the airborne sensors. Table 3 shows that PC 1 only contains 47.99% of the scene's variance, which is quite unusual for spectral imagery.

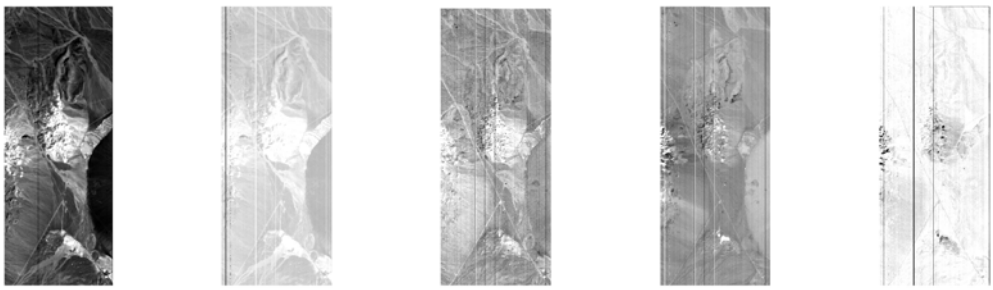

PC1 PC2 PC3 PC4 PC5

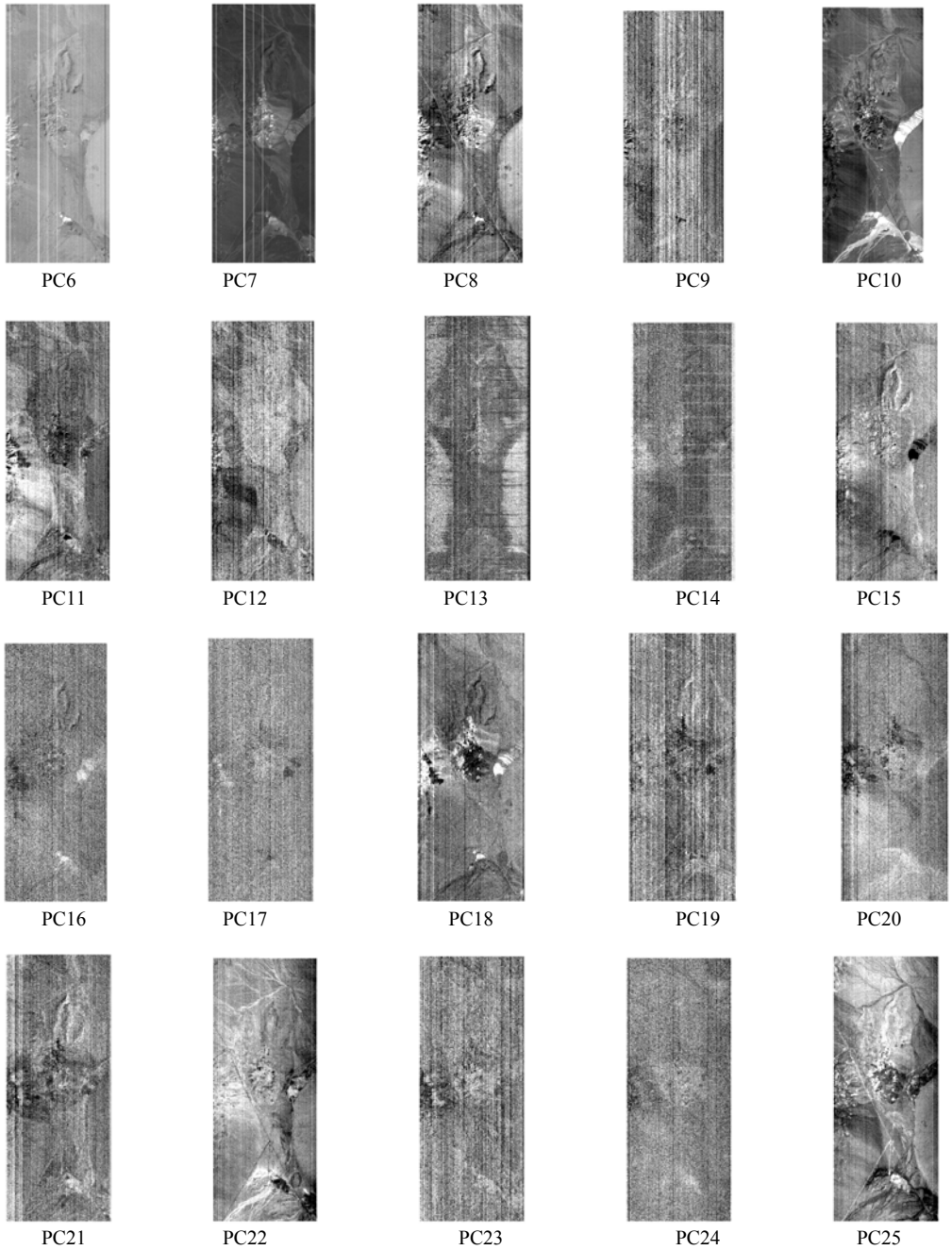

Figure 24. First 24 PC images of Hyperion image data.

For these three image data sets, AVIRIS, HYDICE and Hyperion, the basic PCA transformations lead to similar results. However, some useful points can be brought out concerning the relationship between the quality of data and the basic PCA transformation. AVIRIS data is considered the least noisy of the 3 while the Hyperion data is the noisiest. First of all, the scree test works better on the high quality images

because when excessive noise is present in the data, the eigenvalue curve does not exhibit a single cutoff point but several abrupt changes occur. In the images under examination, AVIRIS data clearly provide one cutoff point in the scree graph, while the Hyperion data, which contain more noise, provide two cutoff points. Additionally, the PC images between the two cutoff points are generally noisy. Second, instrumental noise, resulting in stripping, begins to appear earlier in noisy images, as in the Hyperion data, in which almost all PC images above 2 are noisy. Third, only a few PCs are needed for representation of the image, as higher PC bands depict very little additional information about the scene. This was expected based on the data contained in Table 3 which shows that even when data are noisy, like in Hyperion imagery, components above 10 account for much less than 1% of the total variability of the scene. Finally, the first PCs typically account for different physical properties of the earth's surface. Therefore, a PC band can sometimes clearly represent specific materials, even though the image data under consideration does not represent other materials of the scene very well. For example in AVIRIS data, in the 2nd PC image the streets are distinguished better than in the 3rd PC image, but the intrinsic dimension is determined to be 3 because other scene elements are represented by the 3rd band. This is very important in target detection applications, in which the aim is the enhancement of the contrast for specific materials in the image or, in other words, for information extraction.

3. MNF Transform

The MNF operation is illustrated here for AVIRIS, HYDICE, and Hyperion image data. The images are the same as those used above to illustrate the basic PCA transform. In this application of the MNF transform the noise is estimated using a technique of

PC #	AVIRIS DATA		HYDICE DATA		HYPERIAN DATA	
	Eigenvalue	% Cumulative variance	Eigenvalue	% Cumulative variance	Eigenvalue	% Cumulative variance
1	85531426.539128	81.80	2.2659e+008	80.93	4372.0504	47.99
2	17586259.388255	98.61	4.5947e+007	97.22	876.6685	57.61
3	1076614.573476	99.64	4.1209e+006	98.69	719.4716	65.51
4	151237.433474	99.79	2.5791e+006	99.61	702.1741	73.21
5	75873.569152	99.86	244746.6073	99.83	680.0629	80.68
6	31213.724099	99.89	69675.5509	99.89	661.5558	87.94

7	24944.028624	99.91	40779.5276	99.92	649.3169	95.07
8	20960.387428	99.93	16137.4217	99.94	156.0809	96.78
9	13075.510052	99.95	11186.7101	99.95	115.8653	98.05
10	8905.690938	99.96	7981.7748	99.96	54.8690	98.65
11	6970.305231	99.96	5026.4881	99.96	23.7076	98.91
12	5306.499575	99.97	3271.6278	99.96	15.0095	99.08
13	4679.826547	99.97	3222.4394	99.97	12.3055	99.21
14	4204.588787	99.98	2454.7777	99.97	8.9790	99.31
15	3494.759208	99.98	2345.3105	99.97	6.2356	99.38
16	2186.826167	99.98	2099.9917	99.97	5.9404	99.44
17	1919.274709	99.98	1864.2828	99.97	4.9514	99.50
18	1470.764610	99.98	1628.2456	99.98	4.5587	99.55
19	1307.067302	99.99	1421.5678	99.98	4.3476	99.60
20	1209.950906	99.99	1293.2154	99.98	3.1828	99.63
21	1113.643045	99.99	1237.9501	99.98	2.7205	99.66
22	944.623468	99.99	1013.2552	99.98	2.3373	99.69
23	617.097175	99.99	970.5755	99.98	2.2495	99.71
24	551.599832	99.99	931.0077	99.98	1.9431	99.73
25	464.492358	99.99	863.7067	99.98	1.8763	99.75

Table 3. Eigenvalues and cumulative percentage of the covariance matrix in the basic PCA transform for AVIRIS, HYDICE, and Hyperion images.

differencing of neighbor pixels. This approach assumes that on average, those adjacent pixels contain the same signal, differing only by an amount which is indicative of the noise level. Table 4 presents the eigenvalues and the corresponding cumulative variances for the three images, and Figures 25, 26, and 27 present the first eigenimages for the transformed AVIRIS, HYDICE, and Hyperion data, respectively.

From the AVIRIS MNF transformation results, Table 4 indicates that the first 11 eigenimages are the coherent images, with the remaining eigenimages primarily containing noise. In particular, the eigenvalue for each of the first 11 eigenimages is greater than 5. The eigenvalues for the remaining eigenimages are lower and are all close to one. Per earlier discussion, when using the MNF transform, this is the criterion for setting the dimensionality of the data set. As with the PCA transform, the determination of the inherent dimensionality of the data also requires visual inspection of the eigenimages.

Figure 25 shows that the first two eigenimages have very little integrity as images – a curious feature which seems to be normal for the MNF transform – the first bands are dominated by instrument artifacts, not the desired signal. MNF band 3 shows much higher image quality, and the 4th eigenimage provides a good representation of the scene,

as streets and variations in water depth are well distinguished but ground features are not distinct. In band 5 land cover is distinguished, but variations in water depth are not well represented. Bands 7 and 8 are similar to band 5. The 9th eigenimage is more informative about the overall scene as both land and water depth can be seen clearly. Instrumental noise begins to appear again in band 10 and, from this point on, the image quality slowly decreases. However, the noise level is low enough, until the 22nd eigenimage, that basic features of the scene are distinguishable. Higher number eigenimages contain significant noise and do not appear to provide any more information. The intrinsic dimensionality of the image is determined to be 9 in this case.

The MNF transform for the HYDICE image data results in 15 eigenvalues that are above 5. These bands should contain useful information. Examination of the eigenimages shows that instrumental noise again appears in the first eigenimage, in this case as horizontal stripes. Instrumental artifacts (vertical striping) appear again beginning in eigenimage 5, and although variations in water depth are well represented, the coastline is not clear. Eigenimages contain significant noise from band 8 and up, and the image quality is poor. Finally, the best representation of the overall scene is provided by band 6.

Hyperion data are noisier and the intrinsic dimensionality is 6, based on the eigenvalues of Table 4. Visual observation of the eigenimages shows that instrument artifacts appear again in the first two bands. Additionally, bands 3 to 6 contain vertical striping, but the underlying information is recognizable. From band 7 and up, striping and noise become severe, resulting in poor image quality.

In comparing the MNF and basic PCA transformation results, some useful points can be derived. First, the MNF transformation orders eigenimages in decreasing image quality, excluding the first two images. The first 2 bands contain little scene information. For the standard PCA, higher order PC eigenimages may provide useful scene representations, and local information can be missed when high PC components are discarded.

PC #	AVIRIS DATA		HYDICE DATA		Hyperion DATA	
	Eigenvalue	% Cumulative variance	Eigenvalue	% Cumulative variance	Eigenvalue	% Cumulative variance
1	114.044	22.35	104.919	17.34	34.506	23.75
2	54.113	32.95	42.659	24.43	21.193	38.33
3	26.046	38.05	27.534	28.99	13.328	47.50
4	23.356	42.63	18.257	32.01	9.397	53.97
5	13.650	45.30	14.420	34.40	8.690	59.95
6	11.089	47.48	11.150	36.25	4.621	63.13
7	8.676	49.18	10.297	37.95	2.733	65.01
8	6.985	50.55	8.446	39.35	2.201	66.53
9	6.781	51.87	6.554	40.43	1.789	67.76
10	5.317	52.92	5.954	41.42	1.655	68.90
11	5.025	53.90	5.813	42.38	1.598	70.00
12	4.013	54.69	5.529	43.30	1.452	70.99
13	3.720	55.42	5.409	44.19	1.407	71.96
14	3.512	56.10	5.251	45.06	1.389	72.92
15	2.968	56.69	5.088	45.90	1.324	73.83
16	2.881	57.25	4.710	46.68	1.287	74.72
17	2.748	57.79	4.647	47.45	1.241	75.57
18	2.458	58.27	4.434	48.19	1.193	76.39
19	2.396	58.74	4.388	48.91	1.166	77.19
20	2.164	59.16	4.287	49.62	1.162	77.99

Table 4. Eigenvalues and cumulative percentage of the covariance matrix of MNF transformation for AVIRIS, HYDICE, and Hyperion images.

For these two examples, noise and striping start to appear in lower number components in the basic PCA compared to the MNF transform. For the MNF transform, even high number eigenimages do not contain striping artifacts. This is obvious when comparing AVIRIS and HYDICE images. Even in HYDICE data, in which slight horizontal stripping appears from the first band in MNF transformation, the noise effects are lower in higher number bands in MNF compared with basic PCA. The MNF transform seems to concentrate the instrument artifacts more effectively than the standard PC transform.

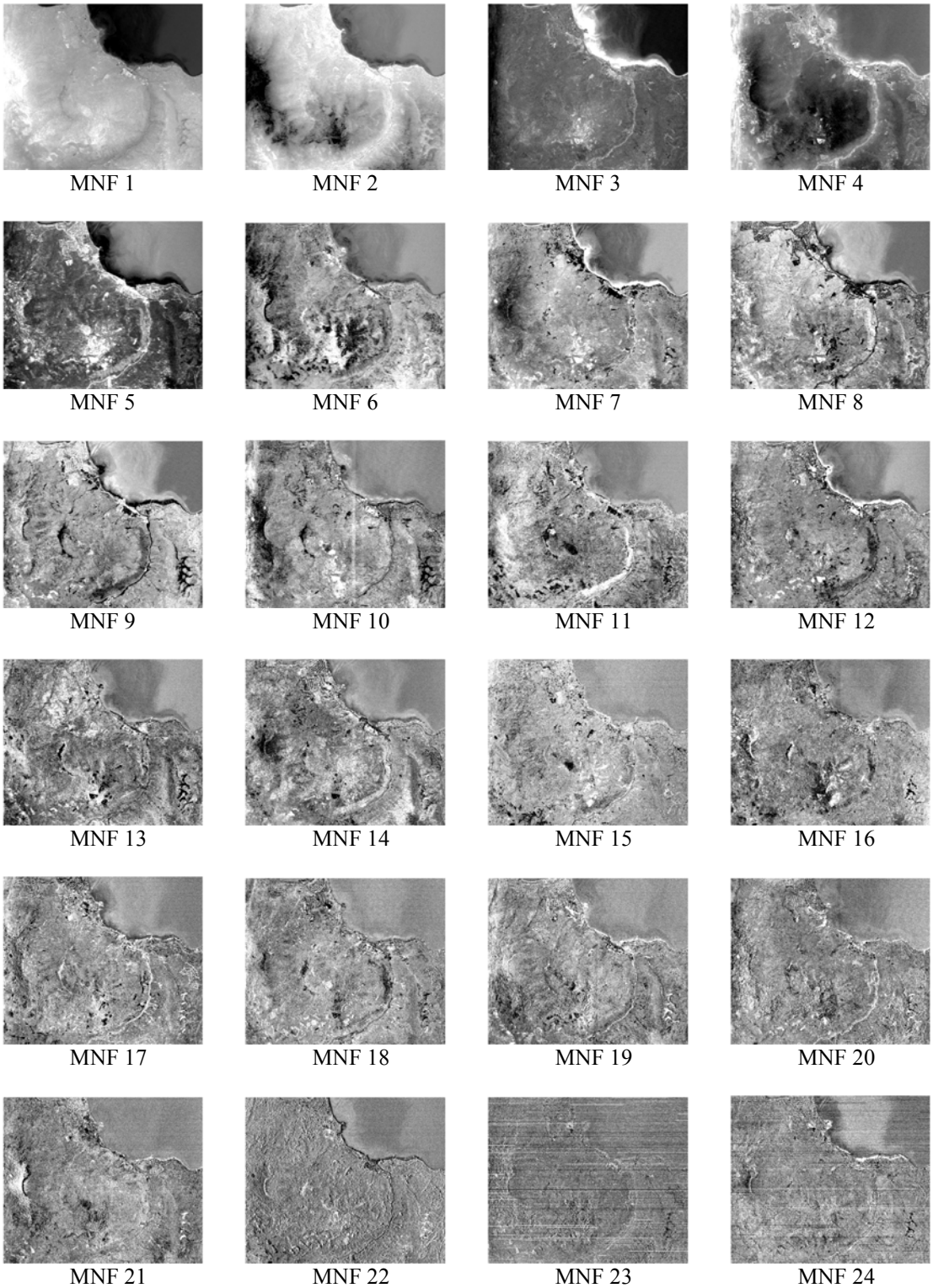

Figure 25. First 24 MNF images of AVIRIS image data.

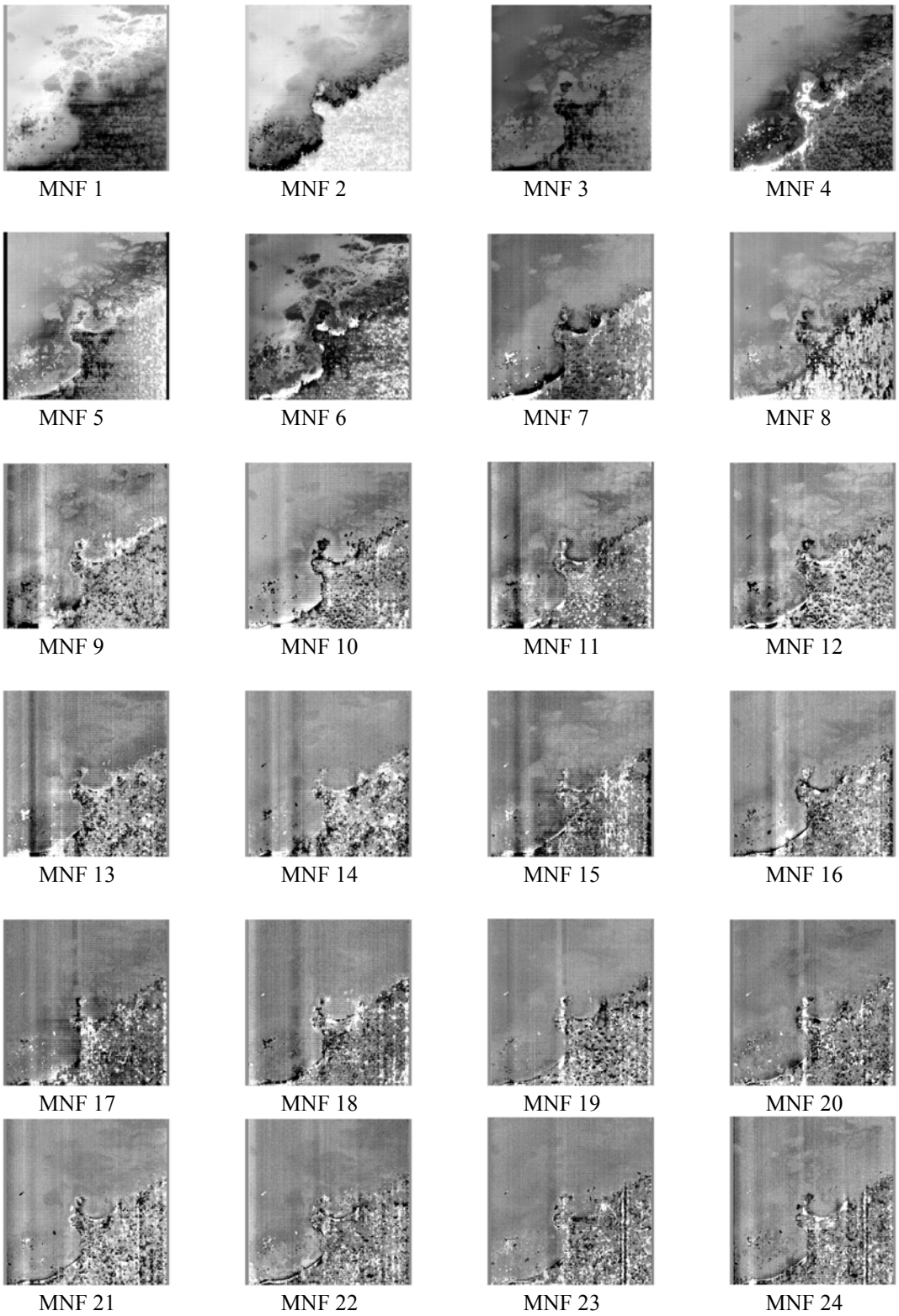

Figure 26. First 24 MNF images of HYDICE image data.

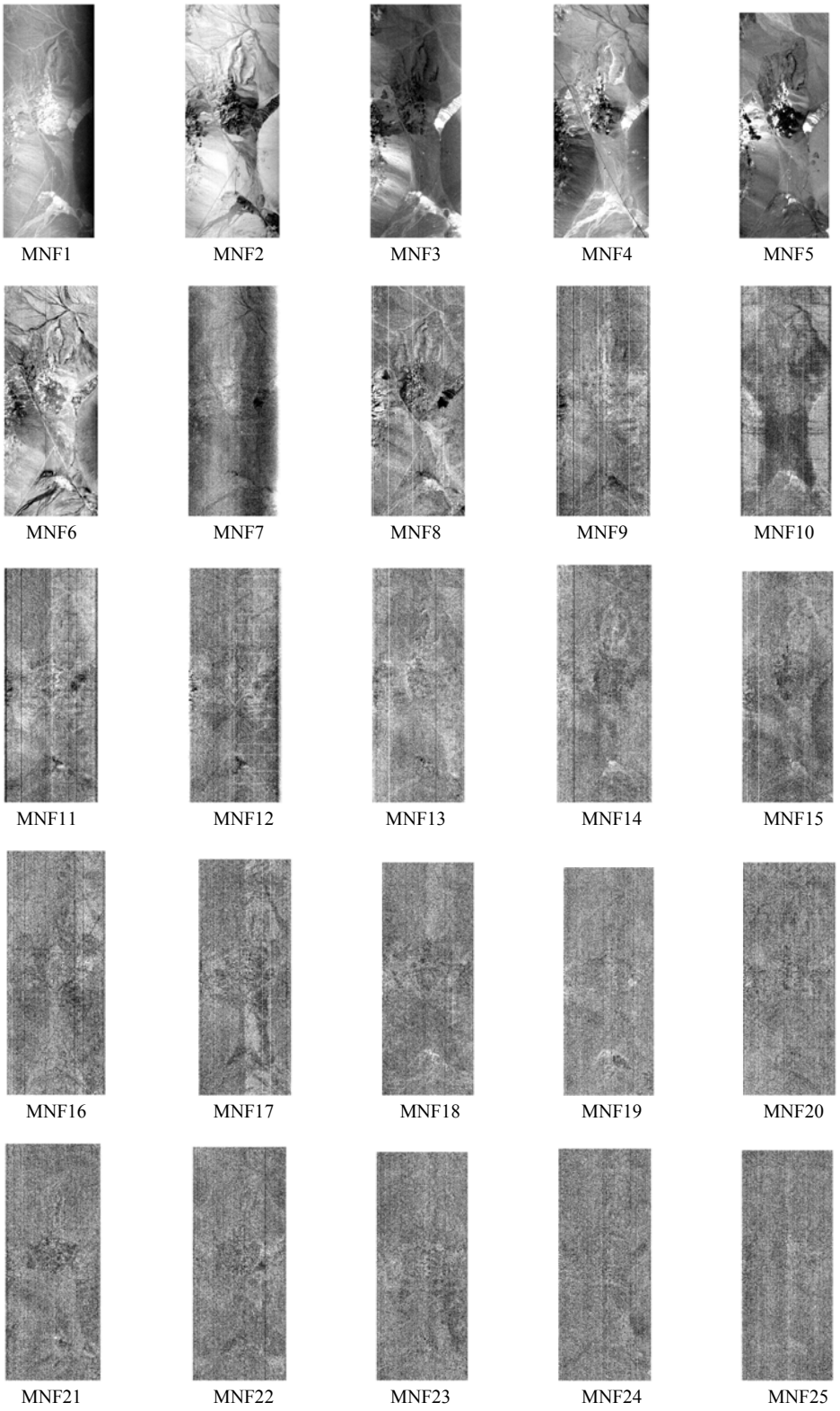

Figure 27. First 25 MNF images of Hyperion image data.

THIS PAGE INTENTIONALLY LEFT BLANK

IV. NOISE REDUCTION USING PCA TECHNIQUES

A. METHODOLOGY

1. Overview

The PCA transformation techniques are examined in this section for their applicability in reducing noise. Noise is induced in hyperspectral image data by several factors such as sensor's sensitivity, thermal effects, quantization errors, and transmission errors. The noise is typically independent of the data and therefore, for the purposes of this thesis, the noise is modeled by adding Gaussian noise to the images. Also, PC techniques are examined for their effectiveness at eliminating striping from hyperspectral data.

A combination of ENVI and MATLAB software was used to construct data sets with varying levels of noise. ENVI was used to manipulate the data into forms that could be easily modified by MATLAB. For example, subset, forward and inversed transformations and conversion of image data in various types (e.g. from Bands Interleaved by Lines (BIL) to Bands Interleaved by Pixels (BIP)) was done using this software. The hyperspectral images were spectrally subsetted and saved in ASCII format. Then, a MATLAB algorithm was used on the image data to add either Gaussian or periodic noise. The noisy images were then processed in ENVI, again using the PCA and MNF transforms. After analyzing the components produced by the transformation, image data were transformed back to the original spectral space. Figure 28 illustrates a general block diagram of this process.

2. Performance Metrics

Two main performance metrics are used in this thesis for evaluation of the retrieval algorithms: visual interpretation and rms correlation coefficient.

Visual interpretation of hyperspectral images involves the observation of differences between targets and their backgrounds, based on some or all of the following visual elements: tone, shape, pattern, texture, and association. Tone is the most important element, as variations in tone allow the shape, texture, and pattern of objects to be distinguishable. Association refers to extracting information about a target of interest by

taking into account the relationship between known recognizable objects. Visual interpretation is widely used because it is a quick method for interpreting the data, but it is not an easily quantifiable approach. Although visual interpretation is a powerful tool for a quick evaluation of the image data, more accurate metrics are necessary.

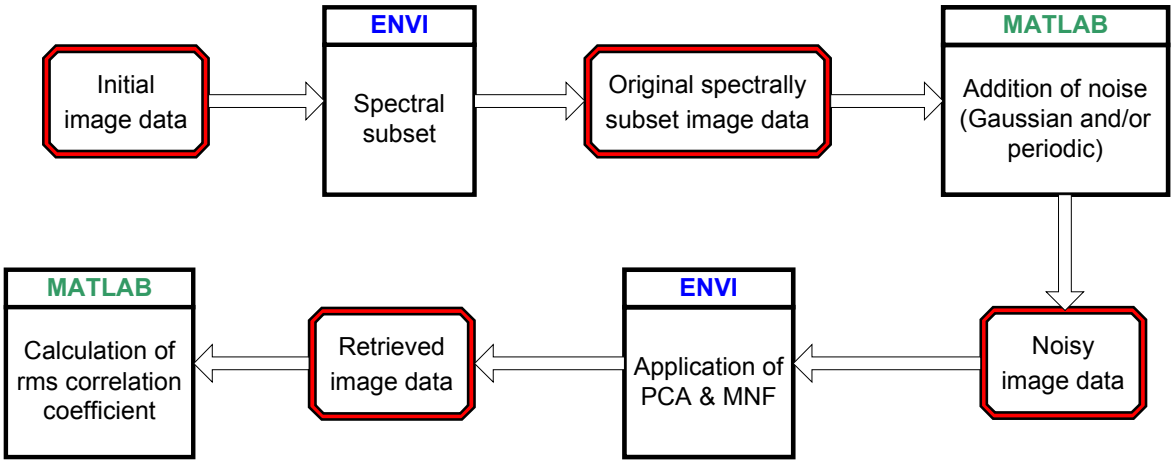

Figure 28. Representative block diagram of noise reduction techniques.

The rms correlation coefficient is a typical quality measure that is used in evaluating the performance of retrieval algorithms for image data. The rms correlation coefficient between two images is calculated by first computing the band to band correlation coefficient between the corresponding bands from the original and the reconstructed image, and then, adding the band to band correlation coefficients and dividing by the total number of bands. This resulting number is the rms correlation coefficient.

In addition to the above performance metrics, spectral comparison and classification are used to characterize the two PC techniques under investigation. Spectral comparison is done for specific areas of interest within the images, comparing the original image data and the retrieved image data. This is done using ENVI areas of interest, or regions of interest (ROI). ROIs are selected and their mean spectra are saved in an ASCII file. These results are imported to MATLAB, and figures containing the spectra of interest are created. Additionally, 2-D scatter plots are used for specific bands

in order to illustrate spectral restoration. Finally, a simple classifier, which is a typical remote sensing method, is used for the purpose of showing the effectiveness of PC techniques in noise removal.

B. IMAGE RESTORATION - RANDOM NOISE

The principal component transform has the characteristic of separating the signal and noise found in spectral imagery. This suggests that the PC transform can be used to remove noise from spectral data. The idea is to perform a forward transform, remove the noisy bands, and then invert the transform. This should remove the noise from the data. In this section the utility of PCA techniques when random noise is present is investigated. The AVIRIS and HYDICE images that were used in Chapter III are again used for the demonstration. The AVIRIS image in this experiment was divided into 65 bands covering the spectrum from 0.4 to 1.0 μm. This was done to reduce the data volume, but does not limit the applicability of the analysis.

The procedure explores the addition of Gaussian noise to spectral radiance image data. Noise at two variance levels, 300 and 600 are explored. Based on the dynamic range of the data, the noise is approximately 10 and 20 percent respectively for the two variance levels. Figure 29 shows the 20th band (588.58 nm) of the original and the noisy images. It is clear that noise, even in the case of a variance equal to 300, is significant and as the variance increases the noise also increases in the image.

The first seven PC's generated by transformation of the original and noisy images are shown in Figure 30. The first PC's produced by the original data are noiseless, and information is depicted clearly. In contrast, starting with the third PC, the PC's produced from the noisy images contain much noise compared to the original PC's.

Noise levels are higher, of course, in the images where the random noise level is higher. The noise appears higher in the PC chain for these noisy data. This was expected because PC images are ranked by variance and hence larger variance of noise means that noisy components will appear in a lower component number in the PC's. Although noise starts to dominate in the third PC, a large fraction of the scene information is preserved in the first two PCs. This is an indication that retrieval of the original image data is possible without losing significant information.

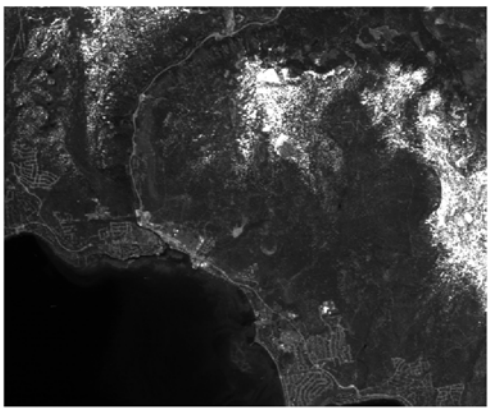

(a)

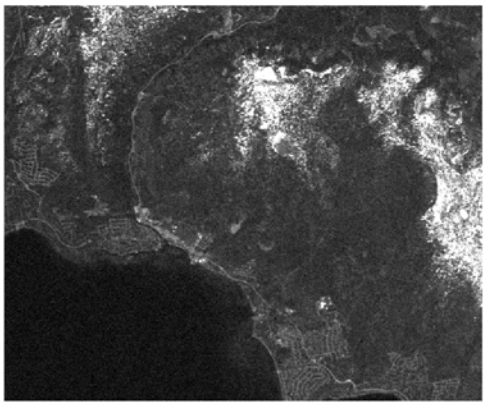

(b)

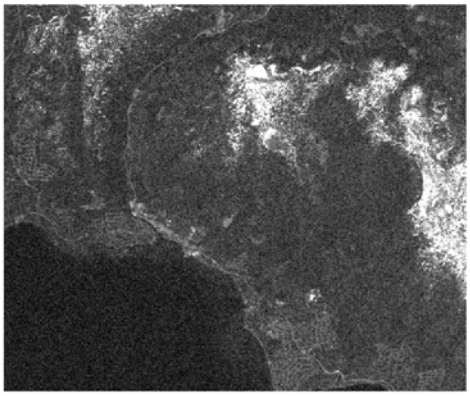

(c)

Figure 29. The 20th band of the AVIRIS images: a) original b) noisy with variance 300 and c) noisy with variance 600.

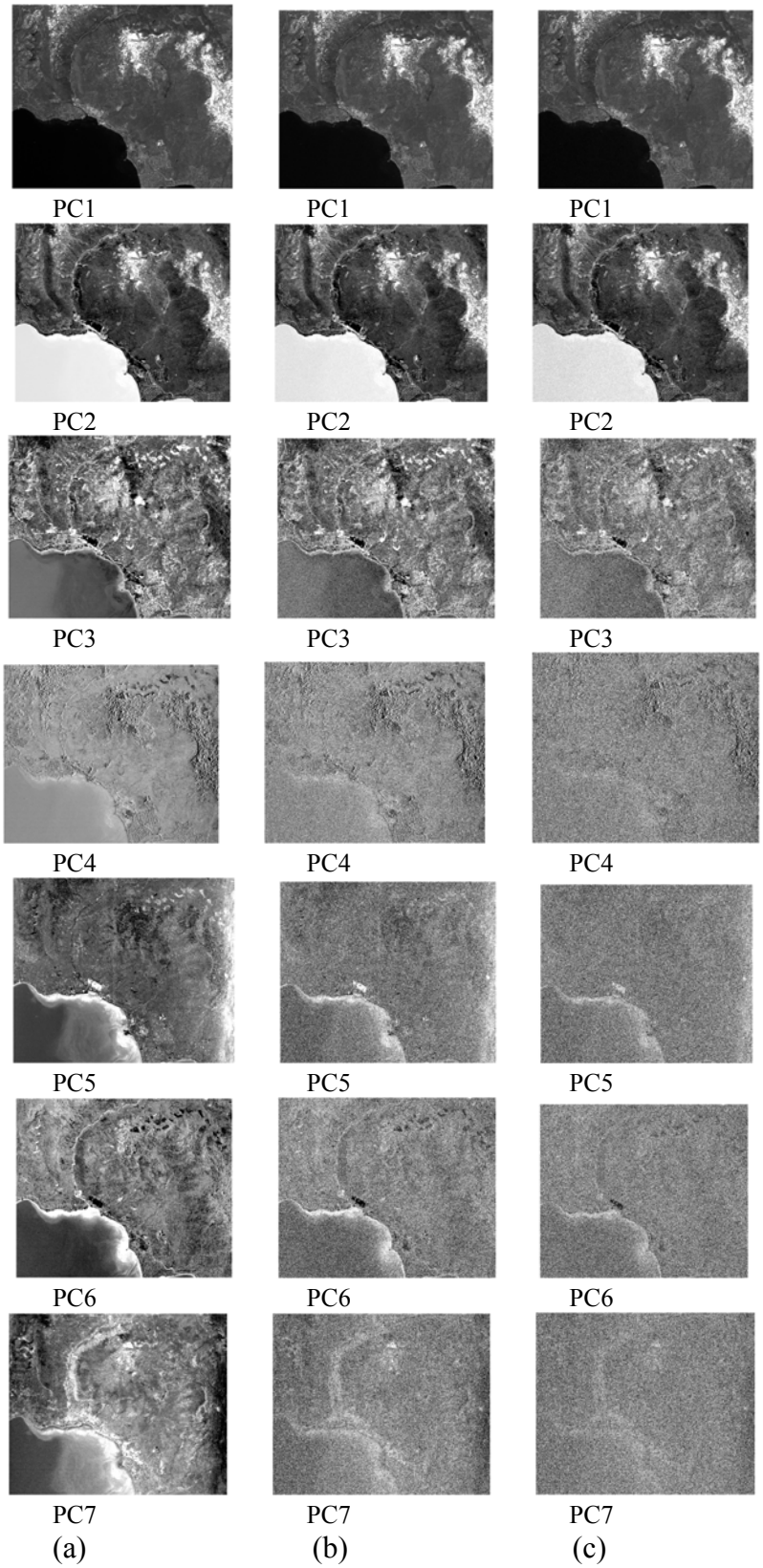

Figure 30. The first 7 PC components of the AVIRIS images: (a) original (b) noisy with variance 300 and (c) noisy with variance 600.

The MNF transform is based on the signal-to-noise ratio of the imagery, so we expect interesting results in tests of the MNF transform as we study the effect of noise. Figure 31 shows the first 7 MNF components produced by the images under investigation. Results are similar to those found for the PC transformation. MNF components 3 to 8 of the original image do not contain noise while noise is significant from the third MNF component on in the noisy transformed images. Also the noise is higher in the MNF eigenimages generated by the data with larger noise variance. Finally, in the first two MNF components, the eigenimages produced from the noisy data show some differences compared to those produced from the original data. In particular, the first MNF component of the less noisy image and the second of the higher noisy image show significant differences in the brightness of the main areas of the scene. The polarity of the scenes has changed. In the first MNF component of the less noisy image, the sea is represented with a dark grey color, almost black, while in the original image it is mostly represented by a light grey, almost white. However, this does not affect the performance of the transformation because the features that are depicted in these MNF components are similar. Figure 32 shows a scatter plot of the MNF first bands between the original and noisy data for a variance of 600. It is obvious that the first two MNF bands are highly correlated, meaning that the first two bands do not contain much noise. In contrast, the original MNF band 3 versus the noisy MNF band 3 are uncorrelated, which indicates that the noisy MNF band 3 is dominated by noise.

Figures 30 and 31 reveal that PC and MNF transformations perform comparably in both low and high levels of noise. The unknown is, again, in estimating the number of components to be used in order to retrieve the original data. Based on both visual observation and the eigenvalues diagram it is concluded that 4 or 5 components must be kept in the case of low variance noise and 2 or 3 in the case of high variance.

Proceeding forward, the inverse transform is applied for 1 to 10 components from the transform space. The effectiveness of the approach is tested by calculating the rms correlation between the original data and the de-noised data. Table 5 presents the rms correlation coefficients between the original and the retrieved data. There is an optimum number of components in each case – too many components cause excessive noise to be

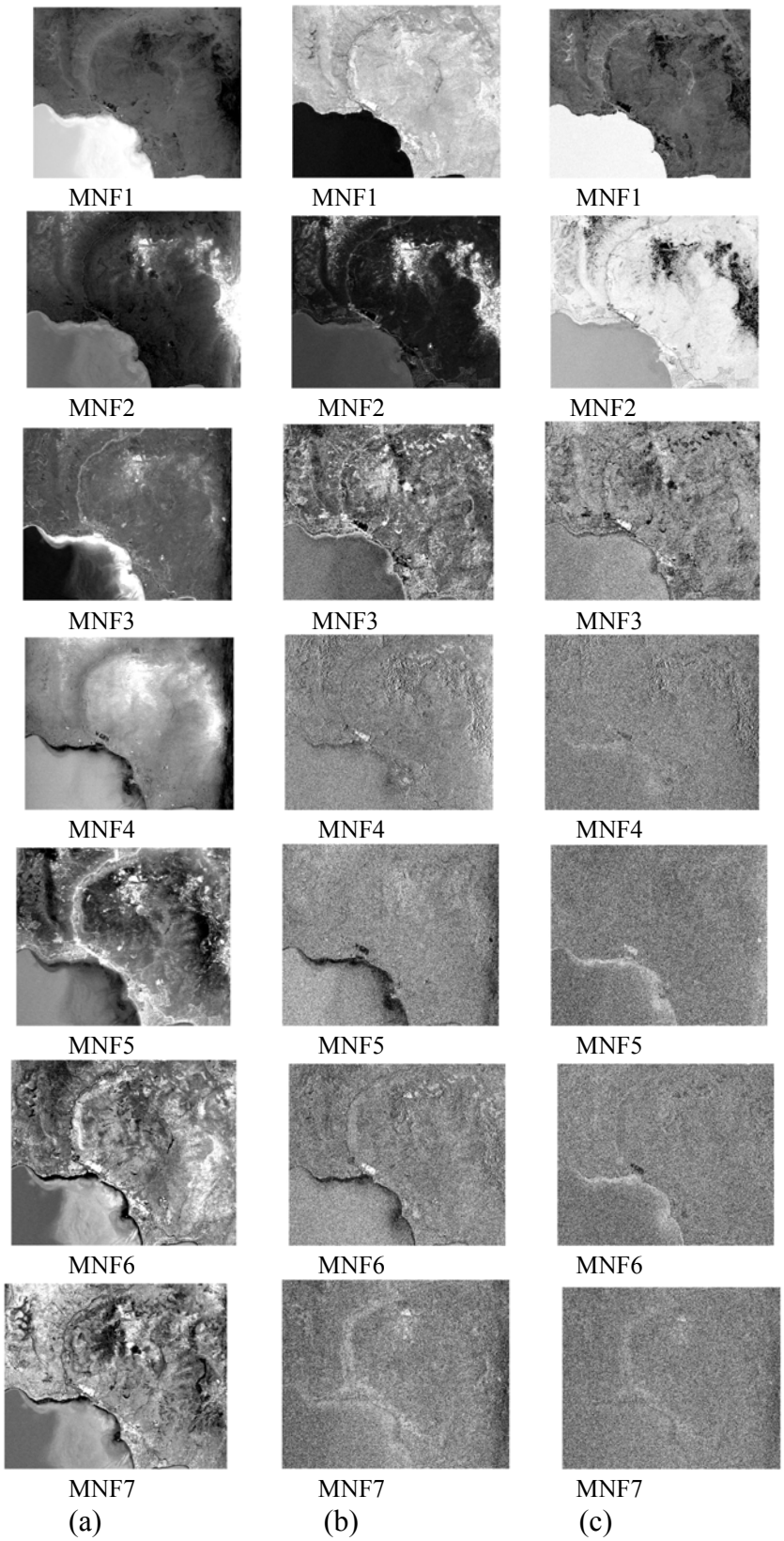

Figure 31. The first 7 MNF components of the AVIRIS images: (a) original (b) noisy with variance 300 and (c) noisy with variance 600.

included. The optimum correlation coefficients for a low-level noise variance of 300 occurs with the 4th PC and 6th MNF components, with values 99.6845 and 99.5760, respectively. Also, in the case of a noise variance of 600 the optimum correlation coefficients occur with the 2nd and 4th PC and MNF components, with values 99.2562 and 98.9743, respectively. The PC transform seems to be more effective than the MNF transform, which is somewhat unexpected. Note, however, that the rms correlation is very low for the case when only the first MNF band is used. Recall that the first MNF band frequently exhibits noise and instrument artifacts.

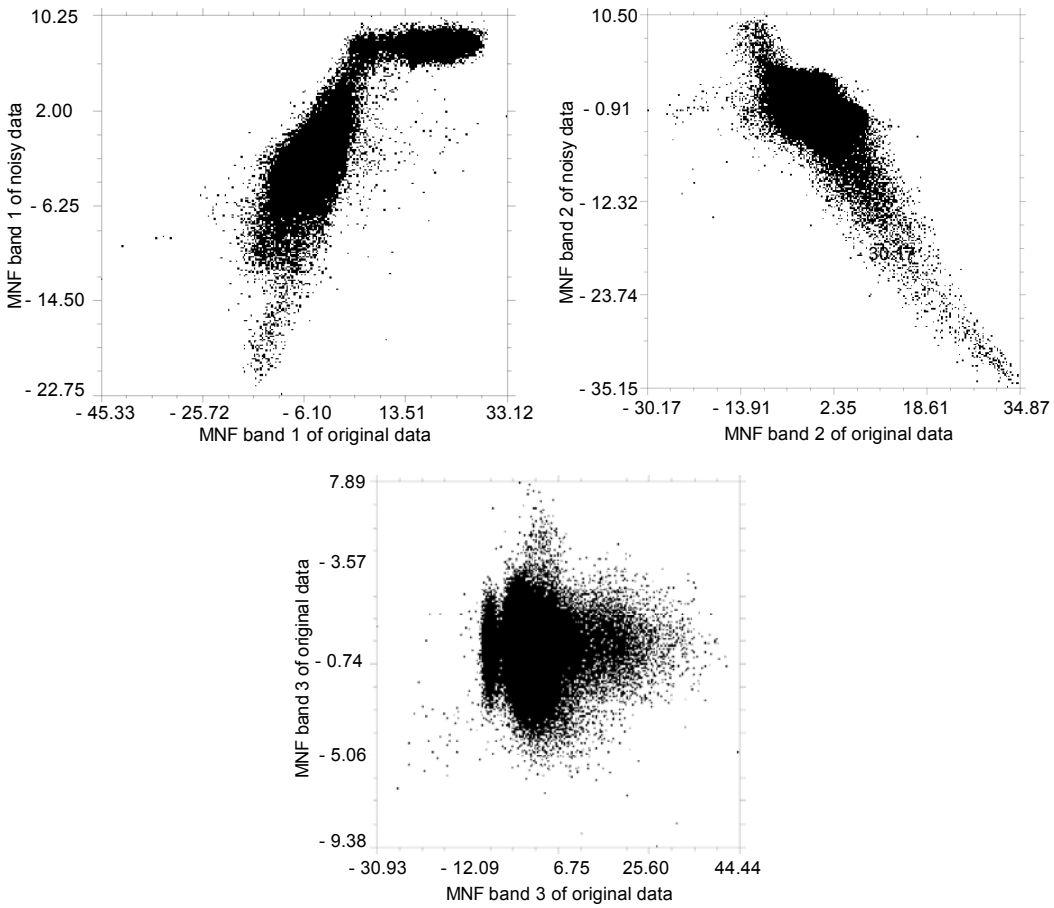

Figure 32. Scatter plots of MNF bands of AVIRIS original vs. noisy with variance 600 image data (a) band 1 vs. band 1, (b) band 2 vs. band 2 and, (c) band 3 vs. band 3.

RMS correlation coefficients				
Number of components retained	**Variance = 300**		**Variance = 600**	
	PC	**MNF**	**PC**	**MNF**
1	91.8515	67.0650	91.6965	74.2586
2	99.5795	98.8010	**99.2562**	98.9469
3	99.6626	99.9400	99.1726	98.9660
4	**99.6845**	99.4766	99.0166	**98.9743**
5	99.6418	99.4412	98.7908	98.7440
6	99.5957	**99.5760**	98.5515	98.5638
7	99.5445	99.5385	98.3240	98.3537
8	99.4712	99.4794	98.0781	98.0978
9	99.3781	99.3662	97.7673	97.8857
10	99.3062	99.2986	97.5310	97.5787
65	96.0710	96.0710	87.2318	87.2318

Table 5. RMS correlation coefficients for original vs. retrieved AVIRIS image data using PCA or MNF transform for two values of noise variance, 300, and 600.

The rms calculation shows the results of the technique on a statistical basis. A more detailed comparison is performed next, by looking at distinct spectra.

In Figure 33, spectra from a region of interest (ROI) in the retrieved, the noisy, and the original images are shown. The ROI is from the open water area of the AVIRIS image. This is a fairly dark region and already has a relatively low SNR. In the blue region (bands 1-20) the AVIRIS data have high radiance values (from 800 to 2,500) while at longer wavelengths (bands 45-65 at 798.46 to 990.53 nm) low radiance values are found (from 0 to 250). Two remarks concerning this figure are worth mentioning. First, the approach used here, with a noise level independent of wavelength, produces a variable SNR as a function of wavelength. For this ROI, there is a dramatic influence above the 45th band while the shape of the spectrum is almost unaffected in bands 1 to 20. The other remark is that both PCA and MNF are effective in restoration of the original spectra. The retrieved spectra for the ROI are very similar to the original as the spikes created from the noise in bands 45 to 65 have been dramatically smoothed. Finally, PCA and MNF perform comparably in performing noise elimination, and it is not possible to make an assessment of which method is better.

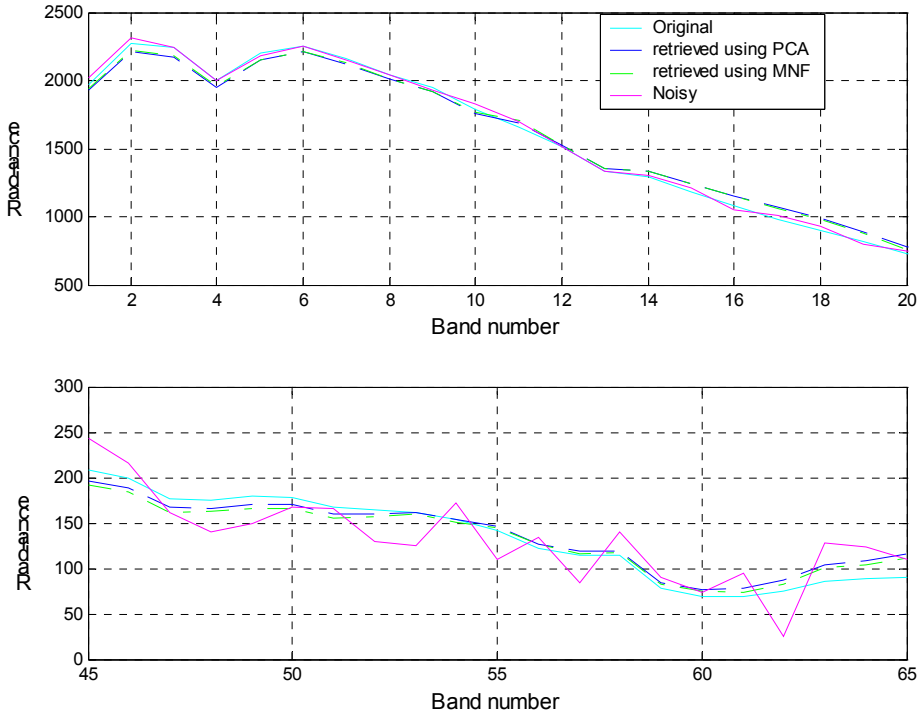

Figure 33. Spectra from an open sea area from the AVIRIS image for the original, noisy, and retrieved spectra using PCA and MNF transformation (bands 1 to 20 (upper figure) and bands 45 to 65 (lower figure)).

The above results for the performance of PC techniques in eliminating noise were duplicated with the HYDICE and Hyperion data. Several cases were examined, as with the AVIRIS data, by adding Gaussian noise. As an example, in Figure 34, the 10th band of the original, noisy, and retrieved HYDICE image data are presented. The retrieved images were obtained using the inverse transform, keeping the 5th and 6th PCA and MNF components, respectively. The retrieved images are good representations of the scene, and important information is clearly depicted, as the noise has been significantly reduced. Finally, both the PCA and MNF transforms perform comparably. Additionally, the above results were confirmed from the rms correlation coefficients. Table 6 shows these coefficients for original versus retrieved HYDICE and Hyperion image data using the PCA or MNF transform for noise variances of 300 and 150, respectively.

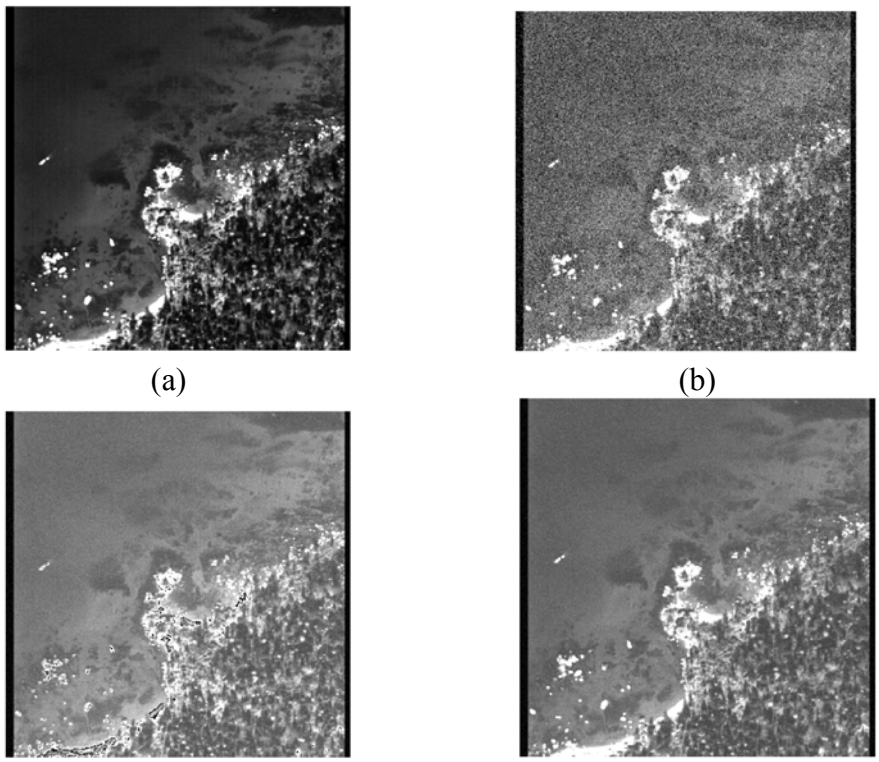

(a) (b) (c) (d)

Figure 34. The 10th band of the follow HYDICE images: (a) original (b) noisy with variance of 300 (c) retrieved using PCA and keeping 5 components and, (d) retrieved using MNF and keeping 6 components.

RMS correlation coefficients				
Components retained	**HYDICE**		**Hyperion**	
	PC	**MNF**	**PC**	**MNF**
1	85.5246	49.8666	58.3970	53N885
2	98.0261	96.4605	59.1403	59.1268
3	98.8128	98.6977	59.2571	59.1499
4	98.9466	98.7680	59.2822	59.1605
5	**98.9947**	98.8416	**59.3903**	59.2111
6	98.7127	**98.9647**	59.3612	59.2279
7	98.5376	98.8122	59.3433	**59.2338**
8	98.3447	98.5583	59.3125	59.2042
9	98.0925	98.2623	59.2603	59.2569
10	97.8417	97.8743	59.2247	59.2053
65	86.6356	86.6356	57.5643	57.5643

Table 6. RMS correlation coefficients for original vs. retrieved HYDICE and Hyperion image data using PCA or MNF transform for noise variance, 300 and 150 respectively.

In the experiments conducted above the noise level was kept constant as a function of wavelength. In this section, the effect of non-isotropic noise is considered. The design of this experiment is to investigate PC methods when noise exists in all bands but is significantly higher in one band. The same subset of 65 bands from the AVIRIS scene is used, covering the spectrum from 0.4 to 1.0 μm. A noise variance of 300 is added to all the bands, except for the 20th band in which noise with variances of 600 and 900 are tested.

Figure 35 shows the first five PC components of the image data for the two cases of higher noise in one band and also for the same level of noise in all bands. In both cases of higher noise in one band the 3rd principal component is dominated by noise while the rest of the components are similar with the components produced when the noise is the same in all bands.

Table 7 shows the rms correlation coefficients for each case. Based on these results, for both PCA cases with anisotropic noise, five components should be retained. This choice gives the retrieved data the closest rms correlation to the original data. By keeping five components, noise is reduced for all bands except band 20. This appears to be due to the noisy 3rd PC. In order for the 20th band to be cleared of noise, the 3rd PC must be excluded. Excluding the 3rd PC not only eliminates the noise from the 20th band, but also raises the rms correlation coefficient. Specifically, when the noise variance in the 20th band is 900, by excluding the 3rd component, the rms correlation coefficient rises to 99.6760 from 99.5540.

Figures 36 and 37 show the impact of the noise/denoise process on the 20th band. Images of the original data without noise (a), with noise (b), and then denoised (c) and (d) are shown in Figure 36. Images are shown for inverse transforms using bands 1-5 and then excluding band 3. Figure 37 shows a scatter plot of the original band 20 and the processed data. The improvement in the correlation is dramatic. The restoration of the original image data is obvious.

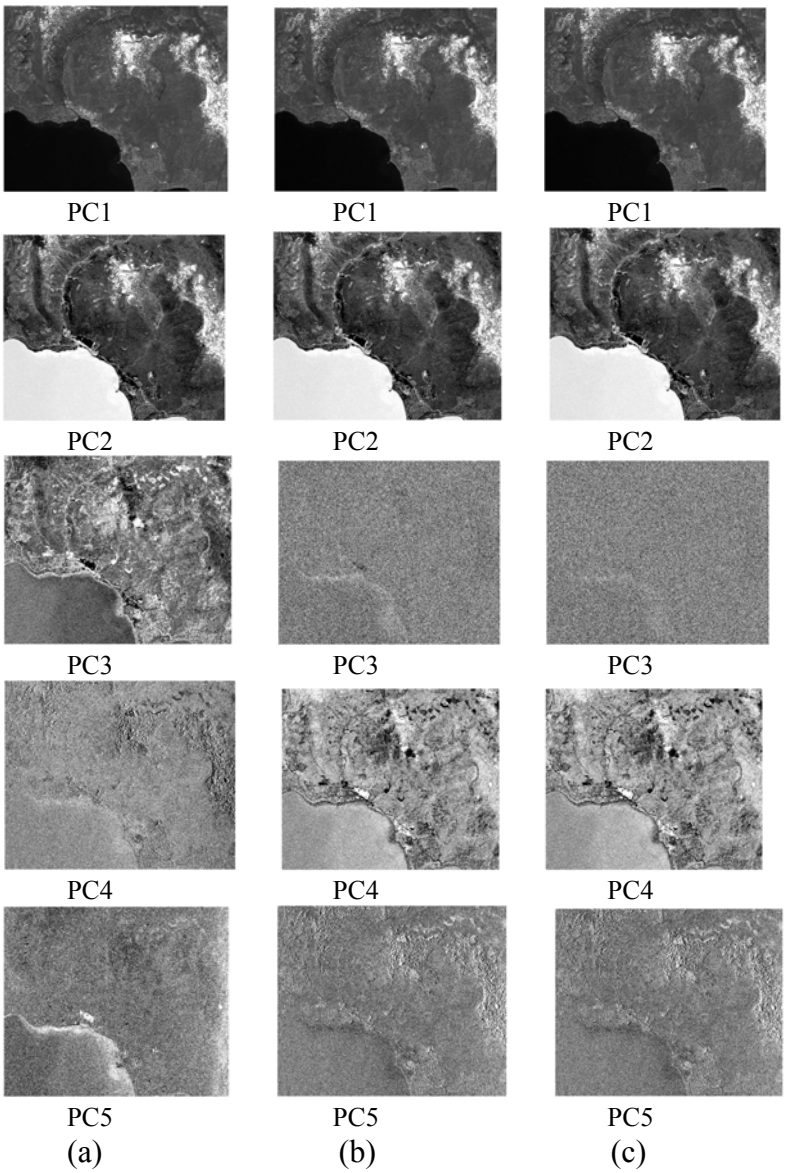

Figure 35. The first 5 PC components of the AVIRIS images: (a) noisy with variance 300 in all bands (b) noisy with variance 300 in all bands except band 20 in which variance is 600 and (c) noisy with variance 300 in all bands except band 20 in which variance is 900.

The effectiveness is also demonstrated by comparing the rms correlation coefficients shown in Table 7. The results are similar to those obtained for the cases of isotropic noise. The correlation coefficients are 99.6847 % and 99.6760 % for the isotropic and anisotropic noise cases, respectively. By contrast, when the third PC component is kept, the correlation coefficient of the retrieved image is lower, with a value of 99.5540. The

difference in the correlation coefficients corresponds to the impact of the 20th band. The 0.122 difference is the difference in correlation coefficients between the original 20th band and the noisy ones with variance of 300 and 600. That means the exclusion of the third noisy PC does not affect the scene information, it omits only the additional random noise contained in the 20th band of the image.

RMS correlation coefficients						
Number of component s retained	**Variance = 300 & in band 20 is 600**			**Variance = 300 & in band 20 is 900**		
	PC 1	**PC 2**	**MNF**	**PC 1**	**PC 2**	**MNF**
1	91.8480	---	67.0543	91.8420	---	67.0520
2	99.5752	---	98.8000	99.5674	---	98.7998
3	99.4528	---	98.9394	99.3246	---	98.9392
4	99.5326	99.6546	99.4878	99.4074	99.6502	99.4895
5	**99.5540**	**99.6760**	99.4631	**99.4291**	**99.6718**	99.4677
6	99.5092	99.6312	**99.5711**	99.3843	99.6271	**99.5700**
7	99.4632	99.5851	99.5346	99.3383	99.5811	99.5337
8	99.4118	99.5338	99.4755	99.2871	99.5298	99.4746
9	99.3186	99.4405	99.3620	99.1938	99.4365	99.3611
10	99.2448	99.4403	99.2945	99.1198	99.3626	99.2934

Table 7. RMS correlation coefficients for original vs. retrieved image data using PCA or MNF transform for noise variance 300 in all bands except of 20th band in which variance is 600 or 900. In PC 1 all the components are retained while in PC 2 the noisy component is excluded.

The MNF transformation also performs well when the noise is higher in one band. In Table 7 the correlation coefficients show that the addition of higher noise in one band does not affect the performance of MNF transformation. In both cases of higher noise, the best correlation coefficient is obtained by keeping six MNF components. Additionally, in the retrieved images the 20th band does not contain noise.

Figure 37 shows the results for both the PC and MNF inversions. The scatter plots, (a) and (b), show that the retrieved 20th band is extremely noisy when the noisy principal component is not excluded – in fact no improvement is found in the inversion process. The noise has not been eliminated. In contrast, the scatter plot (c) between the

original and the PCA transform obtained by excluding the noisy component is a diagonal line which means that this band has been cleaned up. Finally, the last scatter plot shows that in the MNF transform the noise has also been eliminated and thus, the MNF transform performs comparably with the PCA transform when the noisy component is excluded.

In this experiment a basic difference between PCA and MNF has been revealed. That is, the component images in PCA are arranged based on variance, while in the MNF transform they are arranged in decreasing order of image quality. In this case, the variances did not reflect the real SNR due to the disparity of the noise variance in different bands. In the PCA transform, the 3rd component has a larger variance than the 4th component, but it also has a lower SNR.

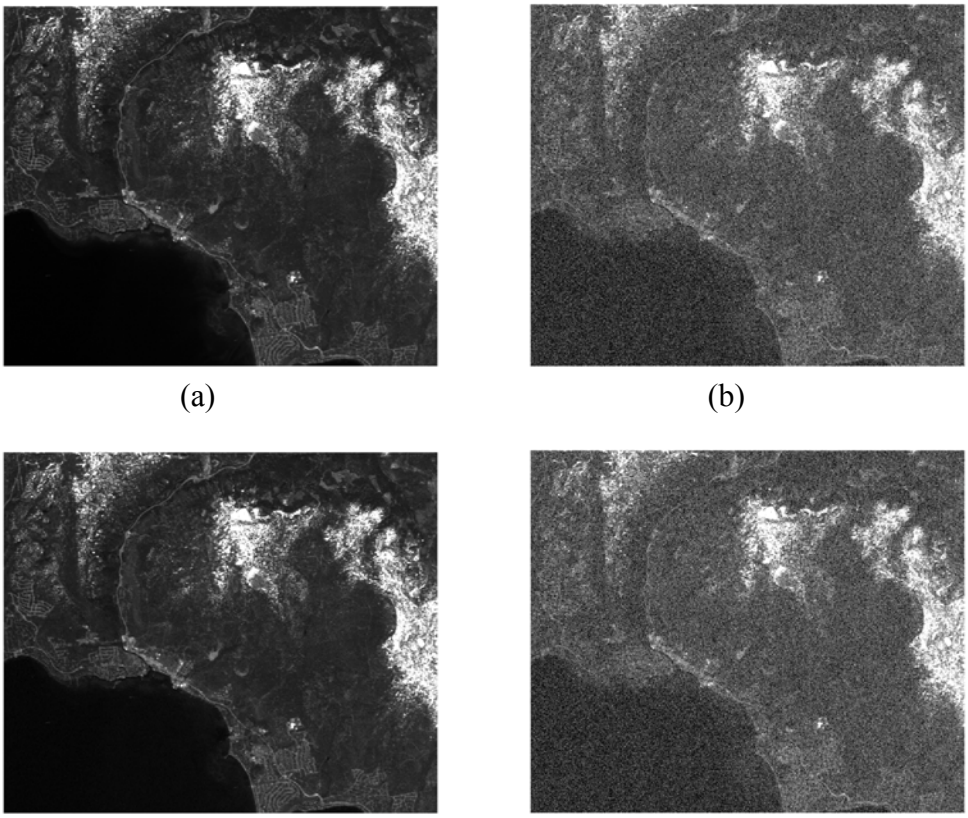

(a) (b)

(c) (d)

Figure 36. The 20th band of the follow AVIRIS images: (a) original without noise (b) noisy with variance 300 in all bands except band 20 in which variance is 900 and (c) retrieved image by keeping the 1st, 2nd, 4th, and 5th principal components (d) retrieved image by keeping the first five components.

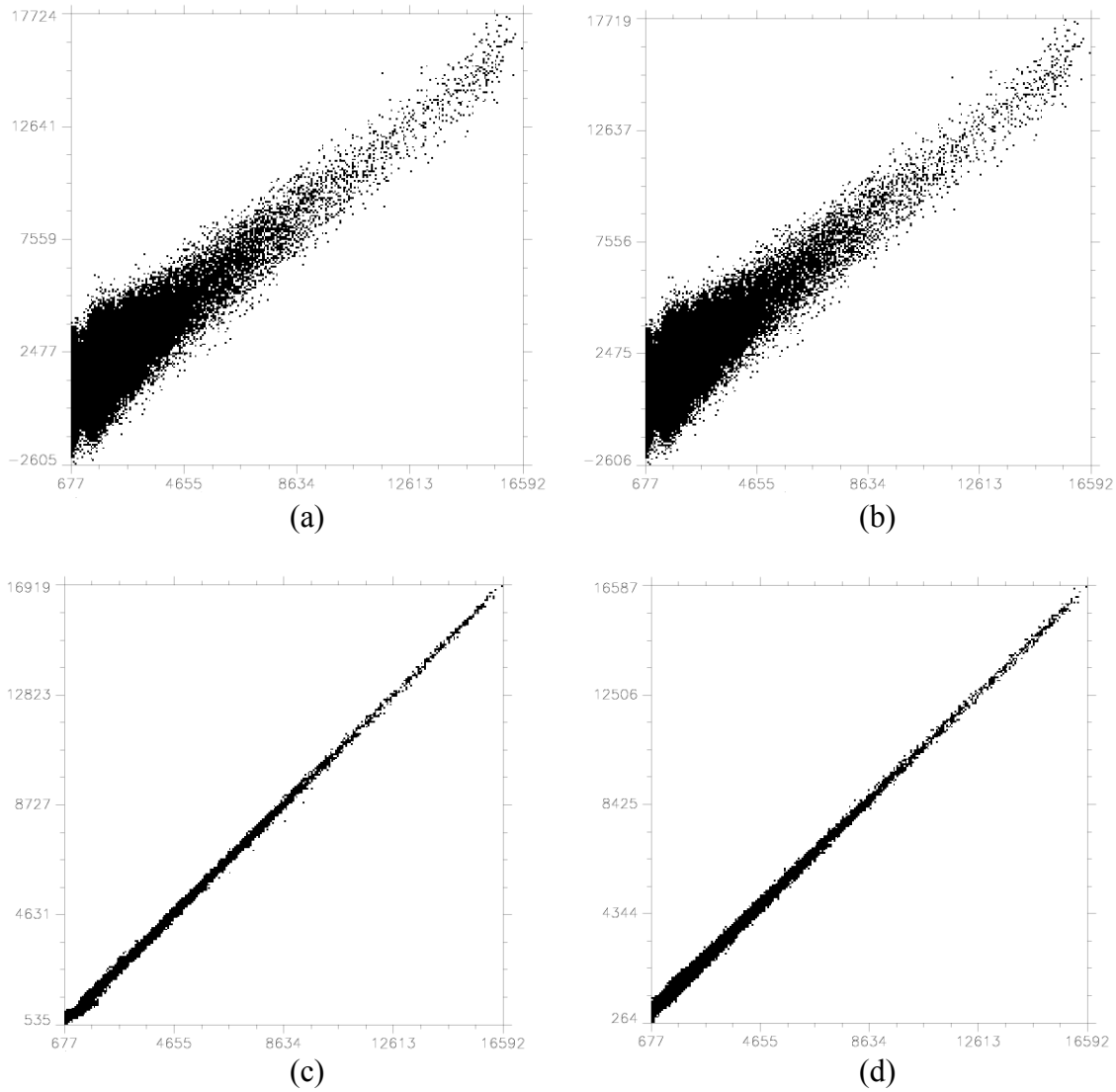

Figure 37. The scatter plots of the 20th band (588.5800 nm) between the original AVIRIS image and the following images: (a) noisy with variance 300 in all bands except band 20 in which variance is 900 and (b) retrieved PCA image keeping the 1st, 2nd, 4th, and 5th components (c) retrieved PCA image keeping the first five components and (d) retrieved MNF image keeping the first six components.

Based on the above discussion, noise removal is effective using PC techniques and generally PC and MNF transformations perform comparably. As a second method of testing the validity of the image retrieval approach, a simple Spectral Angle Mapper (SAM) classifier is tested on the various data sets.

As an illustration of noise removal using PC techniques, Figure 38 shows the original, noisy, and retrieved data using a simple classifier. Five classes are defined, open water, man-made materials, soil, grass, and mountains. The noisy image is the one with a noise variance of 300, and the retrieved image is made by using an inverse PCA transform and keeping five components. The retrieved classified image is similar to the original, while the noisy classified image is very dark, and the discrimination of various features is not possible. Additionally, Table 8 shows the error classification matrix. Each column in the matrices represents a ground truth class, and the values in the column correspond to the classification image's labeling of the ground truth pixels. For example, in the soil class there are 127,943 pixels in the ground truth image. In the retrieved PC image 115,221 pixels have been classified correctly, 1,050 pixels have been classified as man-made material, and 11,672 pixels were unclassified. The overall accuracy - that is the number of pixels classified correctly divided by the total number of pixels - is 87% for the retrieved data and 22% for the noisy data. This means the PC retrieval of corrupted data was successful.

C. IMAGE RESTORATION IN PERIODIC NOISE

PC and MNF transforms are clearly affected by instrumental artifacts, particularly gain/offset errors in focal plane calibration. This type of instrument artifact (along with bad pixels), produces a characteristic striping in push-broom scanners. In this section, the ability of PC techniques to remove undesirable stripping is investigated. Data from AVIRIS are used again. Since the AVIRIS imager is largely free from this artifact, only the striping effects, which are intentionally created, should be present. The subsetted scene is again used, comprised of bands from 0.4 to 1.0 nm. Using a MATLAB algorithm, horizontal lines were added to the images, and correspond either to gain or offset errors. This algorithm creates lines either by adding a constant value or by scaling all brightness values of the pixels of one, or more than one, of the lines in an image. The procedure used above is repeated. The images were transformed to PC or MNF space, the optimum number of retained PC components images were then transformed back into the original space, using the inverse transform, and results were observed.

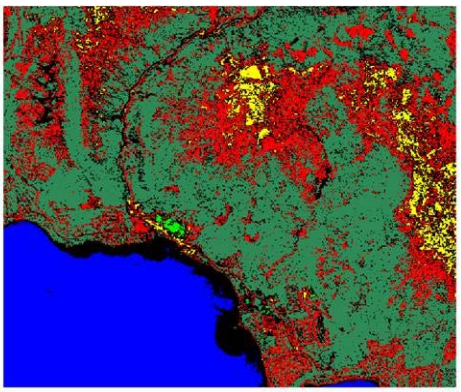

(a)

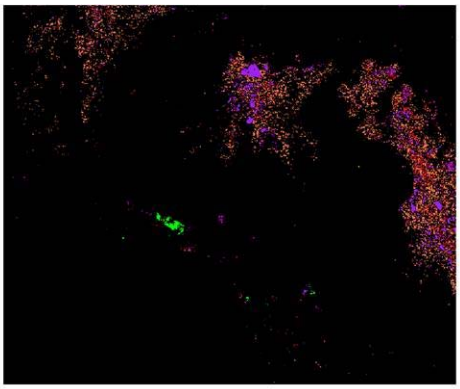

(b)

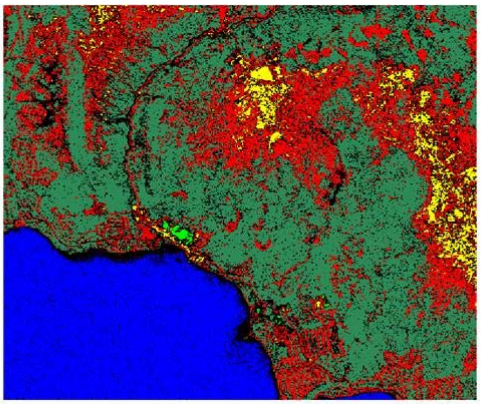

(c)

Figure 38. AVIRIS classification images using a simple classifier: (a) original image (b) noisy image with variance 300 (c) inversed PCA image retaining five components.

For the investigation of gain effects, three different factors were used in this experiment, 1.3, 1.5, and 2.0. Several combinations of different numbers of lines and bands were examined for each factor. For example, in the 20th band (588.580 nm), one, three, and nine lines were added. Also, three lines and nine lines were added to the 50th and 20th bands, respectively. Figure 39 shows the original and corrupted data for the case with lines altered by a gain factor of 1.5. The 20th band is shown in which three horizontal lines have been added.

The transformation of image data to PC space shows that the value of the gain factor and the total number of noisy lines affects the number the of PC component in which lines will appear. For example, in the case of 1 line in the 20th band (588.580

nm), strong lines first appear in the 5th, 6th, and 11th PC components for corresponding factors of 2.0, 1.5, and 1.3. This is illustrated in Figure 40.

CLASS	Unclassified	Manmade materials	Grass	Open water	Soil	Mountains	Total
Unclassified	45775	6179	15	2146	11672	454	66241
Manmade	7647	51551	0	0	1050	0	60258
Grass	21	0	456	0	0	0	477
Open water	4023	0	0	53038	0	0	57061
Soil	5253	802	0	0	115221	0	121276
Mountains	824	0	0	0	0	8241	9065
Total	63543	58532	471	55184	127943	8695	314368

(a)

CLASS	Unclassified	Manmade materials	Grass	Open water	Soil	Mountains	Total
Unclassified	63538	57892	165	55184	127942	2637	307358
Manmade	0	640	0	0	0	0	640
Grass	0	0	306	0	0	0	306
Open water	0	0	0	0	0	0	0
Soil	0	0	0	0	1	0	1
Mountains	5	0	0	0	0	6058	6063
Total	63543	58532	471	55184	127943	8695	314368

(b)

Table 8. Error classification matrix using the AVIRIS original data as ground truth image (a) inversed PCA image retaining five components (b) noisy image with variance 300.

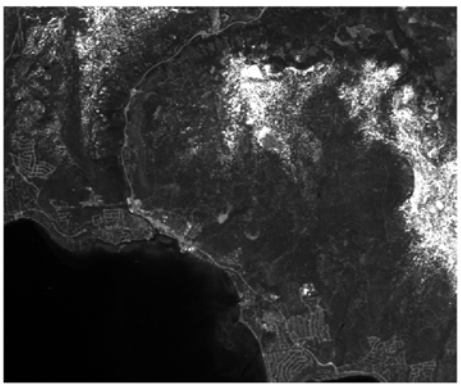

(a)

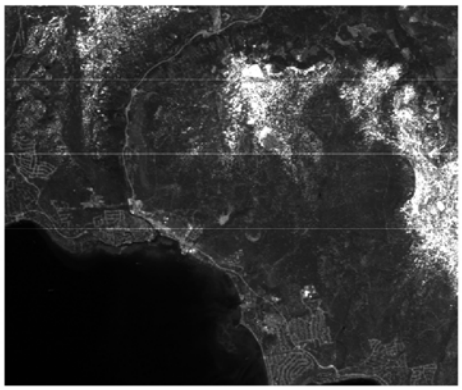

(b)

Figure 39. The 20th band (588.5800 nm) of an AVIRIS image: (a) original image data (b) corrupted image data with 3 horizontal lines of gain factor 1.5.

As shown in Figure 40, in the case of 3 lines in 20 bands from the 11th to 30th band (500.140 to 687.000 nm), a total of 3 x 20 = 60 lines, lines appear first at the 2nd and 5th PC's for corresponding factors of 2.0 and 1.3. Moreover, the lines that appear in the 5th PC, for the case of a gain factor of 1.3, are stronger compared to those that appear in the 2nd and higher components, for the case of a gain factor of 2.0. Therefore, a high gain factor or large number of lines results in lines appearing in lower PC components. Additionally, the number of PC components that can be kept depends on the gain factor and on the number of lines in the test image. This is because retaining PC components that have strong lines will result in these lines also appearing in the retrieved images.

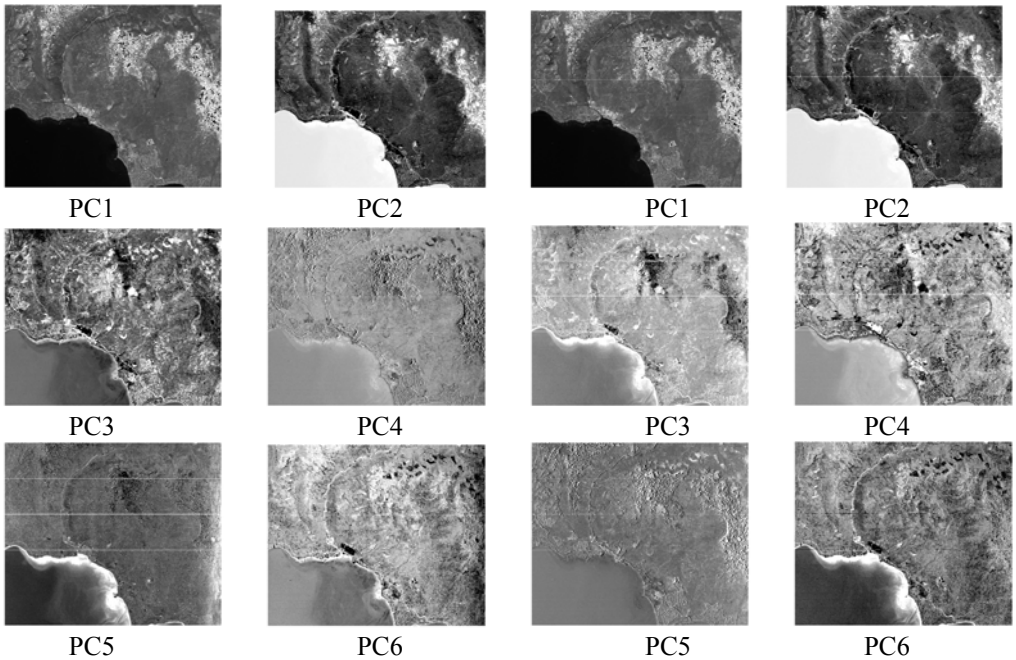

Figure 40. The first six PC components of an AVIRIS image that has been corrupted by three horizontal lines in each band from 11th to 30th for two different gain factors: (a) gain factor 1.3 (the two left columns) and (b) gain factor 2.0 (the two right columns).

On the other hand, the MNF transform shows less sensitivity to variations in the number of lines and the gain factor. In all cases, MNF images yielded strong lines first appearing in the 9th, 10th, or 11th MNF component, irregardless of the number of lines or gain factor. These results indicate that the PC transform does not work as well because,

in order to eliminate striping, only 3-4 PC components can be retained in the inverted image. This low number of PC components may not properly represent all the details in the scene.

As a result, significant information may be lost. The MNF transform performs better, since a larger dimensionality may be retained in that transform space. By keeping the first 8 MNF components, striping is eliminated in the inverted image, and the number of retained components is enough to retain all significant information. The performance of MNF compared to PCA is illustrated in Figure 41, in which the noisy and the retrieved images, for the two different cases, are shown. In this example, the initial noisy image has three striping lines and a gain factor of 1.5, and the MNF image, retrieved by keeping 8 components, does not have any lines. By contrast, the PCA image, retrieved by keeping 5 components for the inverse transformation, is dominated by striping. Additionally, the lines that appear are stronger than the initial lines in the retrieved image using the PCA inverse transform. In both the PCA and MNF, the higher components, usually above the 10th, are dominated by striping.

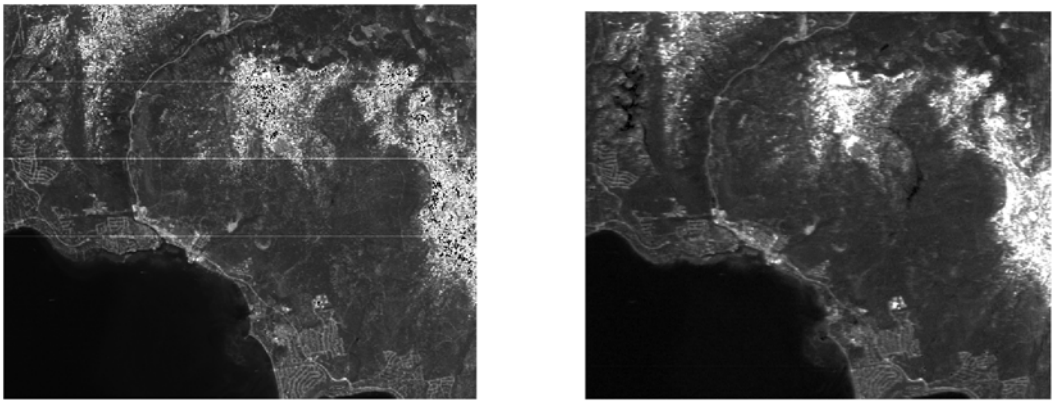

(a) (b)

Figure 41. The 20th band of an AVIRIS image that have been corrupted by three lines in bands 11 to 30 using an offset factor of 2,000. Image data have been restored as follows: (a) using PCA transformation and retaining 5 components, and (b) using MNF transformation and retaining 8 components.

Following the same procedure as above, the impact of offsets was investigated. The same AVIRIS image was modified by adding a fixed value to the brightness values of one or more horizontal lines in the image, using MATLAB code. The addition of a constant value, again, results in striping. Several different combinations of offset values

and numbers of lines were examined. The offset values were +600, +1,200, +2,000, and +3,000 and 1, 3, 9, or 30 lines, in one, or more bands, were created. Figure 42 shows two representative images, corrupted by lines that have been created by adding an offset value.

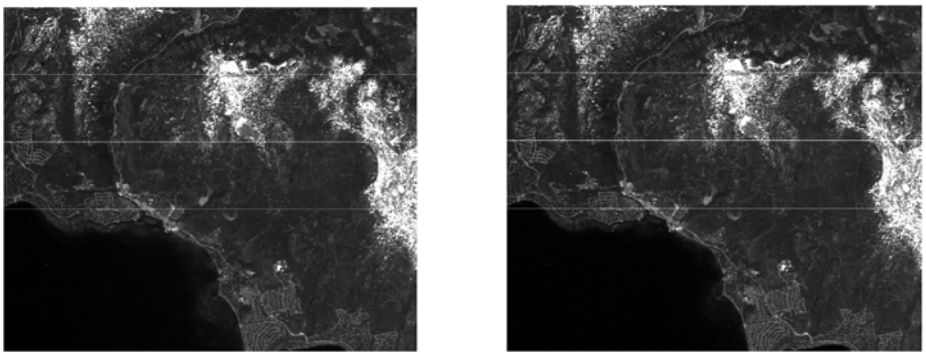

(a) (b)

Figure 42. The 20th band of an AVIRIS image that has been corrupted by 3 horizontal lines with offset values +2,000 and +3,000 for the images (a) and (b), respectively.

Results for offset errors were similar to those found above for errors in gain. In the PC transform, lines appear in early components depending on the number of lines and the offset value. By contrast, for the MNF transform the eigenimages are not as influenced by the offset value or the total number of lines. In all cases, stripes begin to appear after the 8th or 9th component. In Figure 44, the first ten components of PCA and MNF transforms are shown for the AVIRIS image. The data have been modified for bands 11 to 30, by three horizontal lines, with an offset value of 2,000. In the PC eigenimages, slight lines exist in the first two components, while most of the higher components are dominated by strong horizontal lines. Thus, the inverse PC transform leads to a retrieved image that retains striping artifacts. For the MNF transform horizontal lines start to appear beginning with the 9th component.

Inverse MNF transforms with 9 or fewer bands will not have striping. Therefore, as with striping caused by errors in gain factor, the MNF transform performs much better than the PCA transform in elimination of striping. This is depicted in Figure 43, in which, restored image data from the corrupted AVIRIS image, are shown. In the PCA

inverse transform 3 components have been kept but strong lines appear. In contrast, for the MNF transform 8 components are retained, and the retrieved image has no striping. The MNF transform is uninfluenced by the offset value even in case of a huge offset value.

Finally, the ability of PCA techniques to denoise an image when both Gaussian noise and striping exist was investigated. Several cases were examined with hyperspectral images that were modifed by the addition of random noise and horizontal lines. Results indicated that the optimum number of retained components is the smaller component that eliminates both striping and noise. Therefore, when striping is not heavy both the PC and MNF transforms perform comparably. However, when striping is significant, fewer bands can be retained for the PC transform as compared to the MNF transform, and therefore, the performance of MNF is appears to be superior.

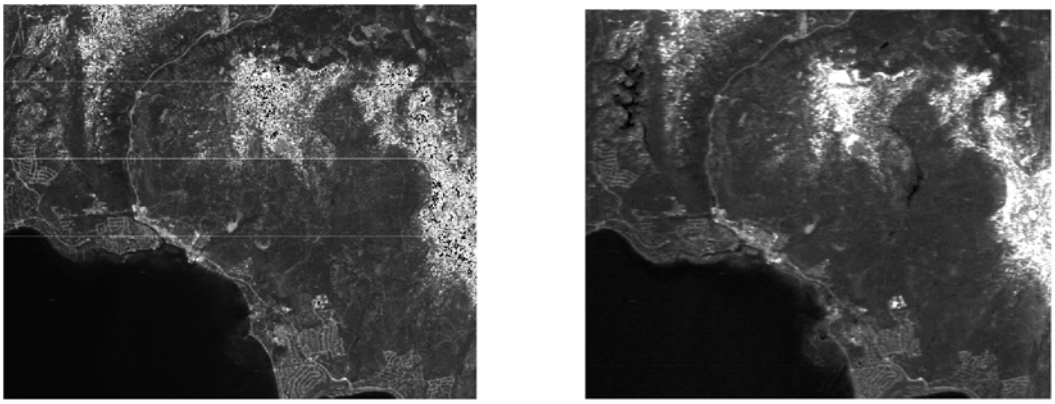

Figure 43. The 20th band of an AVIRIS image that have been corrupted by three lines in bands 11 to 30 using an offset value of 2,000. Image data have been restored as follows: (a) using PCA transformation and retaining 3 components, and (b) using MNF transformation and retaining 8 components.

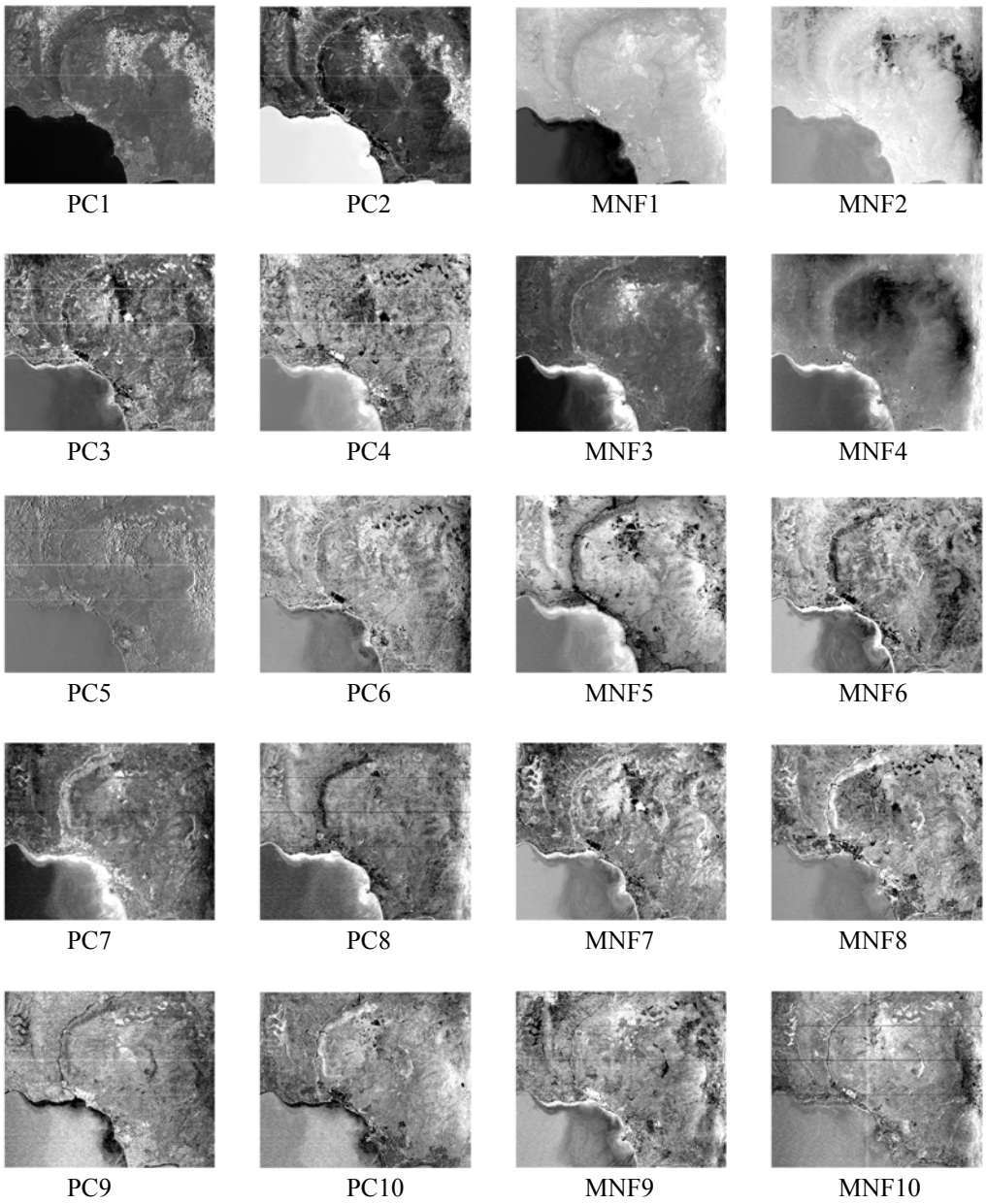

Figure 44. The first ten PCA and MNF components of an AVIRIS image that has been corrupted by three horizontal lines in each band from the 11th to 30th with an offset value of 2,000.

V. CONCLUSIONS

Principal components analysis is a versatile tool in hyperspectral remote sensing which is utilized for various applications such as dimensionality reduction, data compression, and noise reduction. PC and MNF transforms are the two most widely used methods belonging to the PCA family of techniques. In this thesis, an in-depth study of these two methods was conducted in order to estimate their performance on hyperspectral imagery.

The basic PC and MNF transformation were primarily investigated using AVIRIS hyperspectal data. However, for completeness, many experiments were conducted using two other hyperspectal sensors, HYDICE and Hyperion.

One of the research goals was the evaluation of the various methods in determining the intrinsic dimension of the data for the purpose of dimensionality reduction. The results indicate that the scree test gives the best measure of the number of retained components in most cases. The methods of cumulative variance and the Kaiser test seem to perform comparably. By contrast, the CSD method does not perform well, since in all examples, the resultant intrinsic dimension appeared to be too high. When images are quite noisy, all methods seem to fail. For example, in the scree test, when the data are noisy, the determination of the cutoff point is a difficult task. This is because several abrupt changes occur in the eigenvalue diagram. Therefore, visual inspection of the PC images is also necessary both for determining the intrinsic dimension and for better estimation of the components which include useful information.

The analysis also reflected the known tendency for the first component images produced by the transformation to reflect scene topography, shadowing, and broad-band reflectance. Therefore, sometimes a PC image can represent specific materials clearly even though this image does not represent other materials of the scene very well. This is significant in applications like feature extraction and target detection. For the basic PC transform, higher order PC images may better represent image details; data can be missed when high PC components are discarded. This is because basic PCA assumes no *a priori* knowledge of the scene and is concerned only about variances with respect to

decorrelating the data. In contrast, the MNF transform orders component images in decreasing image quality based on SNR.

The performance of PCA methods in noise reduction was examined by corrupting hyperspectral images with noise. First Gaussian noise, which is the most common, was added to those images. The retrieved images, using inverse transforms, indicate that the basic PC and MNF transform perform comparably when noise is white This is reasonable, since the first part of the MNF transform is designed to make the data isotropic in noise (that is noise-whitened). Typically, when using MNF, the optimum number of retained components is higher, but the correlation coefficient between the retrieved and original data is lower.

When one band is significantly noisier than other bands, the basic PC method results in the presence of one noisy component image among the early components, and therefore, this component should be excluded for better results. The inverse PC transform, by excluding the noisy component, does not affect the useful information of the data. It eliminates only the undesirable noise contained in the noisy band. In contrast, when one component is noisier, the MNF transform yields images which are ordered in decreasing image quality. The PC transform arranges bands similarly if the noisy component is excluded.

Second, periodic noise was added to the hyperspectral images using either a gain factor or an offset value. The transformation of image data to PC space shows that the value of the gain factor (or the offset value) and the total number of noisy lines affects the number of PC component in which lines will appear. Specifically, a higher gain factor (or offset value) and higher total number of lines cause striping to appear in earlier principal components. Thus, fewer components can be retained in the inverse transformation. By contrast, the MNF transform showed less sensitivity to variations to the number of lines and the gain factor. Whatever the number of lines and the gain factor was, the first 8 MNF components did not have any striping. The MNF performs better in eliminating the striping compared to the basic PC, because the fewer retained components in the PC inverse transform may result in missing useful information.

Finally, the ability of PCA techniques to clean up an image, when both Gaussian noise and striping exists, was investigated. Both methods eliminated striping and noise in the inverted images, when the retained components were not noisy. The MNF performs better than PC, because more components can be kept when severe striping exists.

THIS PAGE INTENTIONALLY LEFT BLANK

LIST OF REFERENCES

1. Rao, A. K. and Bhargava, S., "Multispectral Data Compression Using Bidirectional Interband Prediction," IEEE Transactions on Geoscience and Remote Sensing, vol.34, no.2, pp.385-397, March, 1996.

2. Richards, J. A. and Xiuping Jia, *Remote Sensing Digital Image Analysis*, Springer-Verlag, New York, NY, 1999.

3. Stefanou M. S., "A Signal Processing Perspective of Hyperspectral Imagery Analysis Techniques," Master's Thesis, Naval Postgraduate School, Monterey, California, June 1997.

4. Diaz, U. A., Reyes, V. M., "Determining the Dimensionality of Hyperspectral Imagery," Laboratory for Applied Remote Sensing and Image Processing, University of Puerto Rico, January 2002.

5. Cattel R. B., "The Scree Test for Number of Factors," Multivariate Behavioral Research 1: 245-276, 1966.

6. Kaiser, H. F., "The Application of Electronic Computers to Factor Analysis," Educational and Psychological Measurement, May 1960.

7. Yury, P. S., "Continuous Measure of Significant Linear Dimensionality of a Waveform Set," Computational statistics and data analysis, June 2000.

8. Green A. A., Berman M., Switzer P., and Graig M. D., "A Transformation for Ordering Multispectral Data in Terms of Image Quality with Implications for Noise Removal," *IEEE Transactions on Geoscience and Remote Sensing*, Vol. 26, no.1, pages 65-77, January, 1988.

9. Shaw G., Manolakis D., "Signal Processing for Hyperspectral Exploitation," in *IEEE Signal Processing Magazine*, Vol. 19, Issue 1, pages 12-16, January 2002.

10. Landgrebe D., "Hyperspectral Image Analysis," in *IEEE Signal Processing Magazine*, Vol. 19, Issue 1, pages 17-28, January 2002.

11. Lee J. B., Woodyatt A. S., Berman M., "Enhancement of High Spectral Resolution Remote-Sensing Data by a Noise-Adjusted Principal Components Transform," *IEEE Transactions on Geoscience and Remote Sensing*, Vol. 28, no.3, pages 295-304, May, 1990.

12. Canada Centre of Remote Sensing, "Fundamentals of Remote Sensing," available at http://www.ccrs.nrcan.gc.ca/ccrs/learn/tutorials/fundam/fundam_e.html, April 2004.

13. AVIRIS Home Page, available at http://aviris.jpl.nasa.gov/, April 2004.

14. Jacobsen Anne, "Analysing Airborne Optical Remote Sensing Data from a Hyperspectral Scanner and Implications for Environmental Mapping and Monitoring," PhD Thesis, University of Copenhagen in Denmark, Copenhagen, May 2001.

15. Harsanyi J. C., Chang C., "Hyperspectral Imagery Classification and Dimensionality Reduction: An Orthogonal Subspace Projection Approach," IEEE Transactions on Geoscience and Remote Sensing, Vol. 32, No. 4, pages 779-785, July, 1994.

16. Olsen R. C., Bergman S., Resmini R. G., "Target Detection in a Forest Environment Using Spectral Imagery," Proceedings of the SPIE Meeting, pages 46-56, San Diego, CA, July, 1997.

17. Barry P., "Introduction to the Hyperion Instrument and Data Processing," available at http://eo1.gsfc.nasa.gov/miscPages/home.html , November, 2001.

18. Berk, A., Bernstein L. S., Robertson C. C., "MODRAN: A Moderate Resolution Model for LOWTRAN7," Hanscom AFB, MA, February, 1989.

19. CSES, Center for the Study of Earth from Space, "Atmosphere Removal Program (ATREM), Users Guide, Version 3.0," Cooperative Institude for Research in Environmental Sciences (CIRES), University of Colorado, March 1997.

20. Larsen R., Nielsen A. A., and Conrandsen K., "Restoration of Hyperspectral Pushbroom Scanner Data," in P.Gudmandsen Proceedings of the 17th EARSEL Symposium on Future Trends in Remote Sensing, pages.157-162, Lyngby, Denmark, June 1997.

21. Goetz A. F. H., Heidebrecht K. B., "Full-Scene Subnanometer HYDICE Wavelength Calibration," Proceedings SPIE, vol. 2821, March 1996.

22. Keshava N., Mustard F. J., "Spectral Unmixing," in *IEEE Signal Processing Magazine*, Vol. 19, Issue 1, pages 44-57, January 2002.

23. Shaheen G. and Rahul J., "Journey into the Atom. Advance Topics in Particle Physics." [http://library.thinkquest.org/10380/advanced.shtml]. 20 December 2004.

24. NASA, "Studying Earth's Environment From Space." [http://www.ccpo.odu.edu/SEES/veget/class/Chap_2/2_Js/2-03.jpg]. 20 December 2004.

INITIAL DISTRIBUTION LIST

1. Defense Technical Information Center
   Fort Belvoir, Virginia

2. Dudley Knox Library
   Naval Postgraduate School
   Monterey, California

3. Engineering and Technology Program Office, Code 72
   Naval Postgraduate School
   Monterey, California

4. Chairman, Code PH
   Naval Postgraduate School
   Monterey, California

5. Dr. Richard C. Olsen, Code PH
   Naval Postgraduate School
   Monterey, California

6. Dr. Daphne Kapolka, Code PH
   Naval Postgraduate School
   Monterey, California

7. Hellenic Navy
   General Staff
   B2 Directorate
   Athens, Greece

8. Leonidas Fountanas
   Lieutenant, Hellenic Navy
   Athens, Greece